ISSN 0736-5306

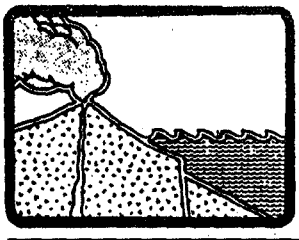

SCIENCE OF TSUNAMI HAZARDS

The International Journal of The Tsunami Society

Volume 14 Number 1 1996

OBJECTIVE: **The Tsunami Society** publishes this journal to increase and disseminate knowledge about tsunamis and their hazards.

DISCLAIMER: Although these articles have been technically reviewed by peers, **The Tsunami Society** is not responsible for the veracity of any statement, opinion or consequences.

Submit manuscripts of articles, notes or letters to the Editor. If an article is accepted for publication the author(s) must submit a camera ready manuscript in the journal format. A voluntary $50.00 page charge ($35.00 for Tsunami Society Members) will include 50 reprints.

SUBSCRIPTION INFORMATION: Price per copy $20.00 USA

ISSN 0736-5306

Published by **The Tsunami Society** in Honolulu, Hawaii, USA

OBSERVATIONS OF TSUNAMI "SHADOWS": A NEW TECHNIQUE FOR ASSESSING TSUNAMI WAVE HEIGHTS?

Daniel A. Walker

School of Ocean and Earth Science and Technology

Hawaii Institute of Geophysics and Planetology

University of Hawaii, Honolulu, HI USA

ABSTRACT

A video recording made on Oahu's northeastern shoreline, as well as eyewitness observations along other coastal areas of the island, confirm the existence of a shadow-type phenomenon associated with a small tsunami from the 4 October 1994 Hokkaido earthquake. These observations suggest that tsunamis in the deep ocean might be detected and measured with optical devices in low-flying aircraft or satellites. Such measurements would be useful in improving the reliability of tsunami warning systems.

INTRODUCTION

The combined effects of a tsunami's propagation in the deep ocean, associated deformations of the ocean's surface, and ocean surface roughness might produce differences in the amount of radiant energy reflected or radiated towards an observer. These differences may be greatest when the energy reflected or radiated at or near the crest of a tsunami wave is compared to the light reflected or radiated from other portions of the wave, making it possible to see a darkened band moving over the ocean surface. A difference in reflected or radiated light has been observed in Hawaii for a small tsunami generated by the 4 October 1994 earthquake near Hokkaido, Japan. The observed "shadowing" effect is associated with a wave height estimated to be only a few centimeters in water depths of about 2 km. [We recognize that the "shadow" is, more precisely, an apparent band of low radiance which is not due to the existence of a shadow. However, for the sake of convenience and consistency with its general perception, we will continue to refer to the phenomenon as a tsunami shadow.] This wave height estimate is based on the fact that there were no reported runups on the island of Oahu in excess of 60 cm. Areas on other islands in Hawaii which, based on historical data, might have been expected to have much higher runups than Oahu, also had no reported values in excess of 60 cm. Thus, an estimate of only a few centimeters in water depths of about 2 km seems reasonable.

THE TSUNAMI SHADOW

Evidence of a tsunami shadow is provided by a video recording made by an observer at Punaluu on Oahu's windward (northeastern) coast. The observer and her neighbors had heard the tsunami warning and moved from their coastal homes to an elevation of about 50 meters above sea level. The footage of the video recorder contains an imprint of the time in hours and minutes, as well

as audio recordings of comments by neighbors of the observer. Local radio personalities who were broadcasting from Oahu's south shore (Honolulu) could also be heard in the background on a neighbor's radio. Comments on the radio indicate that about 12 minutes has to be added to the video time.

At the start of the video, a dark shadow appears on the ocean surface at the horizon extending across the entire field of view of the camera. The shadow is actually a uniformly wide band along the horizon which for some reason is not reflecting or radiating as much sun and sky light as the ocean surface in front of the shadow. Initially, there is no ocean behind the shadow, only sky. However, within a couple of minutes an ocean surface begins to appear behind the shadow which is similar in brightness to the ocean surface in front of the shadow, and the leading edge of the shadow has moved closer to the shoreline. As a few more tens of seconds elapse, the width of ocean appearing behind the shadow increases and the width of the ocean between the leading edge of the shadow and the shoreline decreases (Fig. 1). While the approaching shadow can be seen on the tape, we can also hear an evacuee say: "Look at that son-of-a-gun coming.". . . ."Seven hundred miles an hour." Also, about four minutes after the shadow is first observed on the horizon, you can hear a local radio personality say: "It's already 10:44 and the wave was supposed to hit at 10:42."

As the shadow moved closer to shore, the observers were so concerned for their safety that they turned off their camera in anticipation of possibly having to climb to even higher elevations. Because they were looking down on the ocean, they could not judge the height of the tsunami wave. But from their perspective, its size and speed was terrifying. Based on what they saw their concerns were understandable. Estimates of the speed based on the video recording (elapsed time and distance of travel) and water depth, suggest values in excess of 150 km/hr (i.e., 100 miles/hr). Also, the width of the shadow appears to have been 1 or 2 kilometers.

As it turned out, the observers did not have to move to even greater heights. Although the video was turned off, they noticed that the shadow came all the way inshore until it disappeared as it struck a shallow reef less than 1 km from the coastline. In the hour and a half that the observers remained at the evacuation site, they noticed three other shadows which swept in from the horizon. They were narrower than the first and they were estimated to be at about 20 minute intervals. Other similar observations were made by other eyewitnesses at high elevations on Oahu's north shore and on Oahu's south shore. A summary of their testimony follows.

David Kinolau, Civil Defense Coordinator for District 5 of the City and County of Honolulu, and Craig Huish, a Civil Defense Area Captain, were on a bluff at an elevation of about 100 meters overlooking the ocean on Oahu's north shore. They noticed a dark ocean shadow moving towards shore. Its leading edge was a straight line from left to right as far as the shadow could be seen. They did not recall noticing a trailing edge. As the leading edge moved towards shore, light green water changed to dark blue. As it continued to move towards shallower water the leading edge disappeared near the shoreline. Mr. Kinolau further noted that as the leading edge disappeared, it remained in a straight line and the light green water ahead of the edge began to form a series of small waves with white crests which washed onto the shoreline.

Susan Kennedy was in her Honolulu apartment building at an elevation of about 80 meters. She was looking in the direction of Ala Moana Park, a southwest facing shoreline, at the time, that the tsunami was supposed to arrive and noticed an unusual shadow near the horizon. What was unusual was that the normal ocean was behind it, its leading and trailing edges appeared to be straight lines parallel to the horizon, and it extended as far to the left and to the right as the ocean could be seen. She noticed that there were no clouds. She watched it with binoculars for about 30 seconds. She had been looking at the ocean a few minutes earlier and had not seen the shadow.

Ian Walters was at home at an elevation of about 60 m on Oahu's south shore east of Diamond Head on 4 October. He was on the phone talking to a friend in the late morning when an unusual shadow appeared out of nowhere. It extended to the left and to the right as far as the ocean could be seen. It had straight leading and trailing edges that appeared to be parallel to the horizon. It disappeared when it struck the reef, about 500 to 1000 meters offshore.

DISCUSSION

With a wavelength of many tens of kilometers, what was seen on the video and by other eyewitnesses was only a small a portion of the tsunami's wavetrain. It is not yet known whether the shadow was produced by a portion of its crest, its trough, or its face. In the following, some of the factors which may be associated with this phenomenon are discussed.

In reality the ocean's surface is never perfectly smooth. The "silvery" appearance of portions of the ocean's surface is usually a result of reflections from roughness surfaces appropriately oriented relative to an observer. The effect of ocean surface roughness on observed reflected intensities will depend on the nature of that roughness. Roughness can range in wavelength from millimeters to kilometers, encompassing small wind-driven wavelets or ripples to ocean swells and tsunamis. Roughness is seldom, if ever, totally random because it is produced by a variety of non-random forcing functions (e.g., currents, winds, storms, and earthquakes).

Considering reflected energy, whether a rougher or smoother ocean will reflect more energy will depend on the relative locations of the sun and the observer, as well as the nature of the ocean surface roughness. Considering radiated (i.e., unreflected) energy, ocean surface roughness could also affect the amount of energy available for scattering and absorption within the body of the ocean, as well as the amount radiated directly from surface particles.

The crest of a deep-ocean tsunami is the highest point of a deformed ocean transmitting energy along the sea-air interface at speeds of hundreds of kilometers per hour. Water particle motions at the sea-air interface associated with these high transmission rates could serve to increase ocean surface roughness, especially at the crest where the compressive forces of adjacent particles due to gravity are at a minimum. Whether such changes in roughness could be easily observed by an individual is questionable because of the long wavelengths of tsunamis. However, interactions of receding and incoming waves could produce steeper, shorter period waves in which changes in roughness might be more readily apparent to an observer. Like large ocean swells, such tsunami waves could then be seen out in the ocean before they strike coastal areas. [Updrafting air currents can also change the surface roughness of wave faces and contribute to optical differences which permit their identification.]

Increasing of ocean surface roughness by water particle motions along portions of a tsunami's wavetrain could be perceived as a shadow. We speculate that the tsunami shadow observed in Hawaii for the 4 October 1994 tsunami may have been produced by an increase in ocean surface roughness which lowered the amount of skylight reflected toward the observer from the ocean's surface along the crest of the tsunami. Other explanations also associated with water particle motions, at or below the surface, may be possible (e.g., absorption or scattering effects). Numerical modelling of tsunamigenically induced water particle motions on ocean surface roughness, reflectivity, and radiation could be useful in evaluating such speculative interpretations.

Such modelling is required for computations of radiance transfer functions for rough ocean surfaces (e.g., Preisendorfer and Mobley, 1986; Mobley, 1989; Gordon and Wang, 1992; Mobley, 1994). In addition to all the complexities associated with these simulations, "tsunami shadow" modelling would require consideration of the water particle motions associated with the transmission

of tsunamigenic energy at rates of up to 220 m/sec. Indeed, differences in the characteristics of these motions at different points of inflection along the wavetrain may provide important clues in the determination of the physics involved in these observations. Further insights regarding the possible nature of the "shadow" are provided by C. D. Mobley (author of Light and Water, 1994), who upon viewing the video provided the following commentary (personal communication, 3 March 1995).

> "I found the video fascinating. I think that the shadow phenomenon is almost certainly due to a steepening of capillary wave facets on the water surface, induced by the tsunami wave. If the capillary waves steepen, then an observer looking at a nearly horizontal line of sight (as is the case here) will see reflected light from higher in the sky than is the case for less steep capillary wave slopes. This is the same thing you see when a gust of wind makes a "cat's paw" on the water surface. On a clear day, the cat's paw appears darker than the undisturbed water because it is reflecting a deeper-blue sky light. It is well known that internal waves can induce small changes in capillary wave slopes, which make the internal waves visible at the sea surface as alternating "slick" and "rough" bands. I see no reason that tsunamis could not do the same thing. On the other hand, I cannot imagine that a tsunami could change the inherent optical properties of the water itself in any significant way. In other words, I think the effect shown on the video is purely one of sky light being reflected differently by the sea surface as the tsunami passes by."

IMPLICATIONS

Differences may not be restricted to sunlit (or moonlit) ocean surfaces. Even at night there may be differences in the photon count that could be measured with sophisticated optical devices. However, lines of sight that are nearly horizontal to the ocean's surface may be required. The singular importance of the 4 October 1994 tsunami shadow is that it was produced by such a small amplitude in relatively deep water. Destructive Pacific-wide tsunamis could have similar amplitudes in the deep-ocean, and the width of their shadows could be directly dependent on the tsunami's deep-ocean amplitude. Also, a tsunami's destructive potential is directly related to its deep-ocean amplitude. Therefore, it might be possible for low-flying aircraft or appropriately located satellites, to track the tsunami out in the deep-ocean and provide estimates of its destructive potential well in

advance of its arrival in populated coastal areas.

Considering the cost of false warnings in terms of inconvenience, disruptions of the economy, and the potential erosion of credibility in the warning system as well as other government agencies, with consequential losses of life, further investigations should be undertaken to evaluate the potential of deep-ocean "shadows" as possible indicators of tsunamigenic potential.

ACKNOWLEDGMENTS

Awareness of this phenomenon for such a small tsunami might not have been possible without the video recording of Dolores Martinez. We thank Merlyn Pickering for advising us of the existence of this video and we thank Dolores Martinez for sharing her observations with us. We also thank Craig Huish, Susan Kennedy, David Kinolau, and Ian Walters for supplying independent confirmation of similar observations elsewhere on Oahu. The comments and suggestions of Curt Mobley, who reviewed a draft of this paper, are also greatly appreciated and may be of critical importance in understanding the phenomenon. This is SOEST Contribution 4075 and Hawaii Institute of Geophysics and Planetology Contribution 880.

REFERENCES

Gordon, H. R. And M. Wang, 1992. Surface-roughness considerations for atmospheric correction of ocean color sensors. I: the Rayleigh-scattering component, *Appl. Optics*, **31**(21), 4247-4260.

Mobley, C. D., 1989. A numerical model for the computation of radiance distributions in natural waters with wind-roughened surfaces, *Limnol. Oceanogr.*, **34**(8), 1473-1483.

Mobley, C. D., 1994. Light and Water, Academic Press, New York, 592 pp.

Preisendorfer, R. W. and C. D. Mobley, 1986. Albedos and glitter patterns of a wind-roughened sea surface, *J. Phys. Ocean.*, **16**(7), 1293-1316.

Figure 1. The tsunami "shadow" can be seen just below the horizon and extends across the entire field of view of the camera. Approximately 12 minutes has to be added to the time indicated based on simultaneously recorded audio of a local radio station. The video was taken at an elevation of about 50 meters above sea-level.

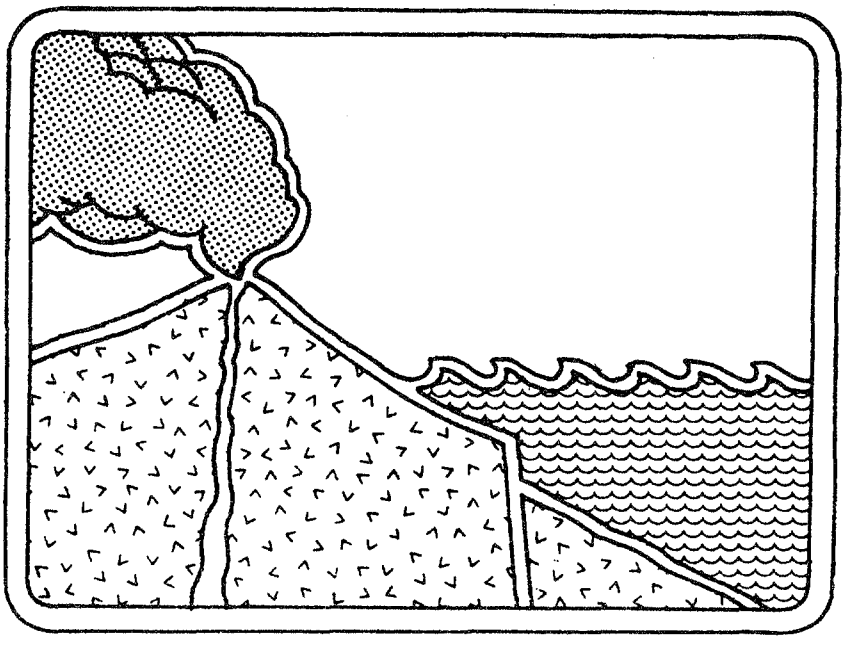

NUMERICAL MODEL FOR TSUNAMI GENERATION DUE TO SUBAQUEOUS LANDSLIDE ALONG A COAST
- A case of the 1992 Flores tsunami, Indonesia -

Fumihiko IMAMURA
Disaster Control Research Center
Tohoku University
Aoba, Sendai 980-77, Japan

Edison C. GICA
School of Civil Engineering
Asian Institute of Technology
G.P.O.Box 2754, Bangkok 10501 Thailand

ABSTRACT

A tsunami model including the motion of a landslide using a circular-arc slip model and a subsidence model is proposed, and applied to wave generation for the case of the significant phenomena in the southern shore of Hading Bay, Flores Island, Indonesia. One-dimensional propagation and simple topography are introduced to simplify the numerical condition because of the lack of field data. A highly accurate method independent of spatial grid size to calculate a sea bottom deformation is proposed. The effects of soil diffusion, bottom friction and drag on the wave generation are also discussed. The results of this research suggests that two circular-arc slip model properly describes the significant phenomena at the Hading Bay.

1. PROBLEM IDENTIFICATION

On 12 Dec. 1992, at 0530 GMT or 1330 CIT (Central Indonesian Time), an earthquake with a magnitude of Ms 7.5 struck Flores Island, Indonesia with epicenter located at 8.482°S, 121.930°E, approximately 50 km northwest of Maumere, the center of Flores Island. About 2,000 people were killed by the earthquake and tsunami. Seventeen days after the earthquake, an International Survey Team gathered information from 29 December 1992 - 5 January 1993 **[YEH et al.(1993)]**. From the survey conducted, the measured values were significantly greater than the predictions by numerical simulation **[IMAMURA and KIKUCHI(1994)]** at some points:Uepadung, Waibalan, and Riangkroko (see Figs. 1 and 2). Also the survey brought about several problems such as liquefaction and landslide.This paper will discuss one of the problems encountered by the survey team which is the significant phenomena in the southern shore of Hading Bay.

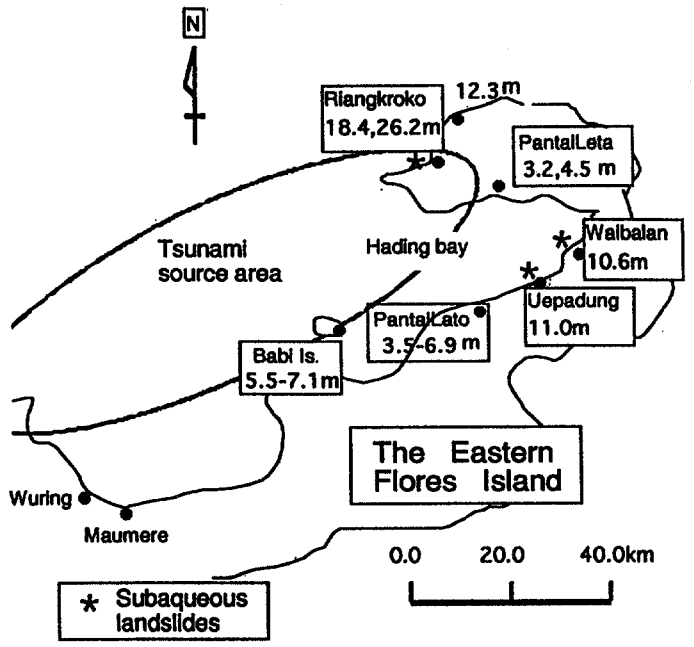

FIGURE 1 Measured tsunami heights on the eastern Flores Island and estimated tsunami source. The locations of subaqueous landslides are also shown (After Imamura et al., 1995).

On the southern shore of Hading Bay, near Uepadung, massive subaqueous slumps were found (see Fig. 3 and Photos 1 &2). The slumps were almost vertical and caused the disappearance of approximately 150 meter wide and 2 kilometer long shoreline. The visual observation of the run-up height was 14 meters. Two more landslides were found at Lewobele, approximately 6 kilometers west of Uepadung, each 1 kilometer long. Landslide and ground deformation also occurred further west at Pantal Lato, but with no significant subaqueous slump and an average tsunami run-up height of 3.4 meters was measured, much smaller as compared to that in areas with subaqueous slumps.

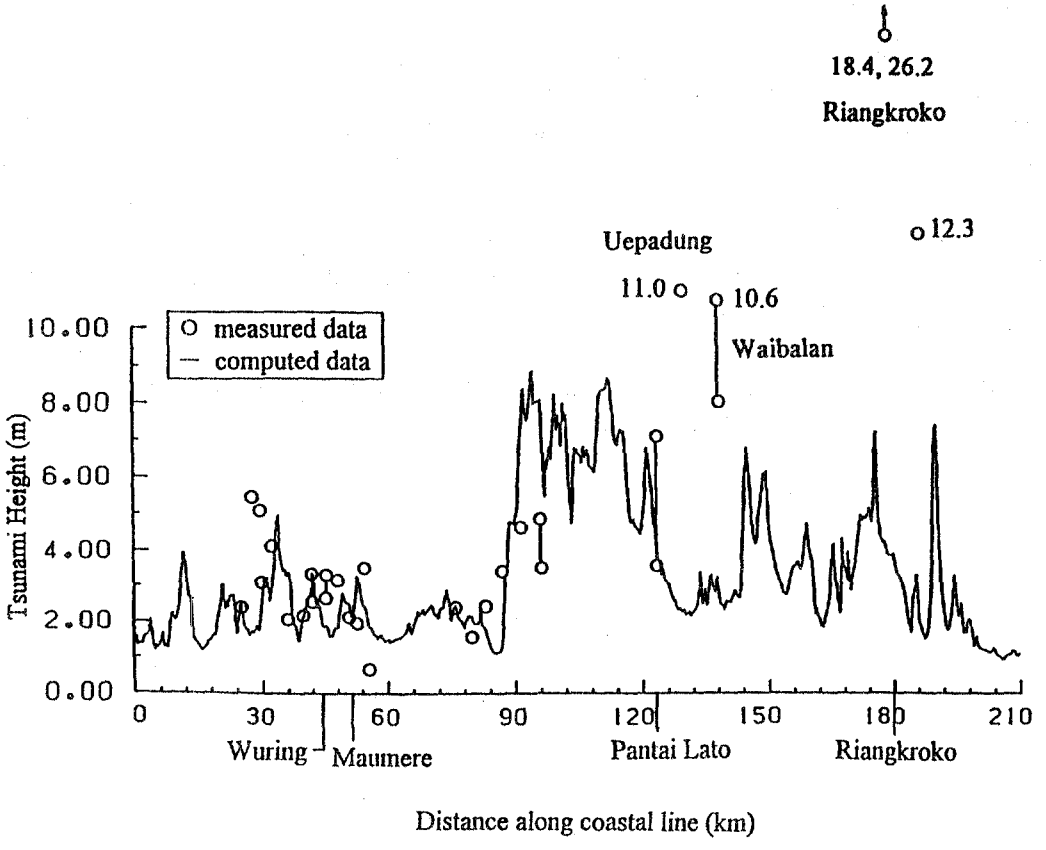

FIGURE 2 Comparison between the measured run-up heights and the computed maximum water level along the northern coast of Flores Island (After Imamura et al., 1995). The discrepancies bewteen measured and computed runup heights are significant at Uepadung, Waibalan, Riangkroko in the estern Flores Island.

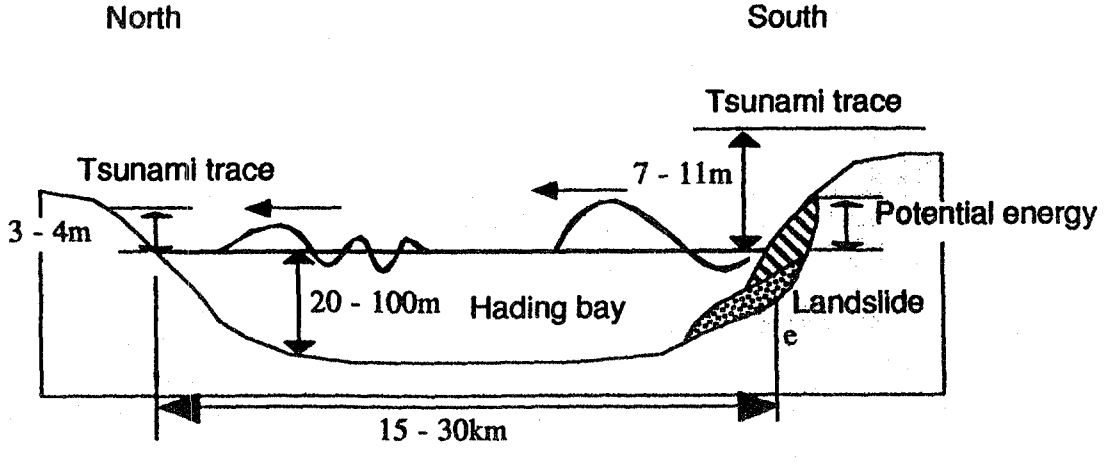

FIGURE 3 Sketch of tsunami generation and propagation in the Hading bay interpreted by the result from field investigation. Large tsunami runup heights nearby the landslide and smaller one at the opposite coastal line were found.

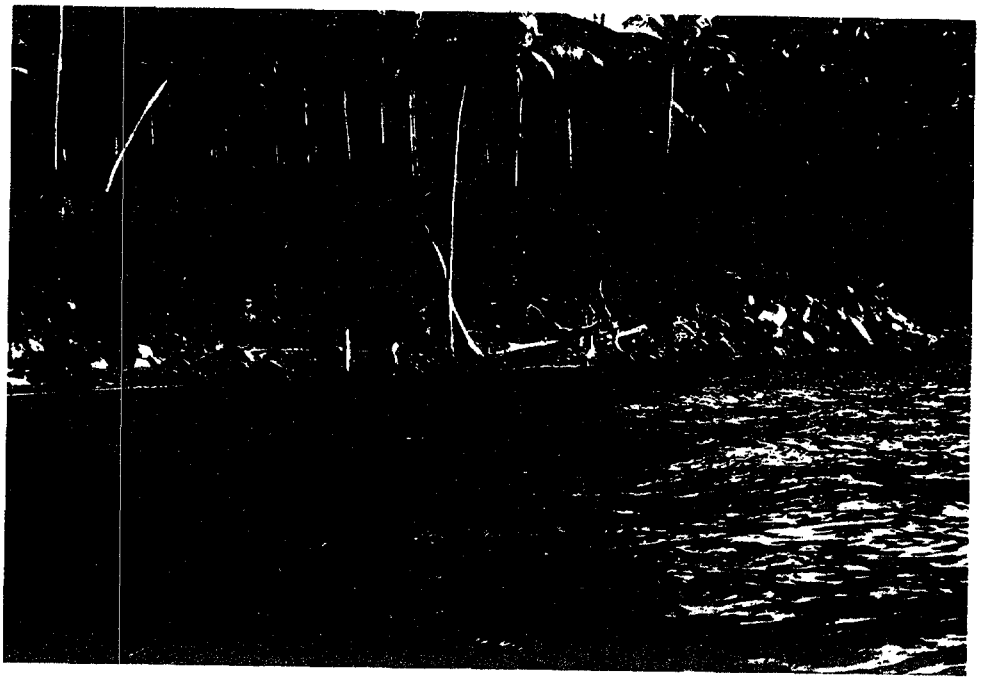

PHOTO 1 Landslide found at Waibalan. The cliff of 8 -12 m height is 150 m wide and 2 km long.

PHOTO 2 Landslide found nearby Riangkroko. Although the survey and measurement of the landslide scale could not be done on the site, its height was estimated to be more than 30 m

Surprisingly, the maximum run-up height, 10-11 m, along the north shore of Hading Bay, at the opposite side of Uepadung where no significant subaqueous slumps were found and only 4.3 meter of tsunami runup height was observed shown in Fig.3. This indicates that the large run-up heights were limited to the area around subaqueous slumps and might be caused by submarine-landslide generated waves rather than tectonic tsunami waves. However it was not clear whether tsunami arrived before or after the slumps, it was noted from the interview of the survivors that the tsunami attacked few minutes after the earthquake, while the arrival time estimated by the simulation was more than ten minutes.

At some plàces the detailed computational results of the Flores Island tsunami were significantly smaller than the measured values. The numerical simulation was based on a 300 x 300 meter grid which is enough to reproduce the tsunami and give good agreements with the measured values **[IMAMURA et al., 1995]**. The above facts suggest that the wave was generated due to local effects, that is subaqueous landslide. However, so far the simulations **[AIDA(1961) and IMAMURA (1995)]** have not properly included the wave generation due to landslide, but that of tectonic activity.

Further research was, therefore, conducted for the case of the significant phenomenon on the southern shore of Hading Bay, by simulating numerically wave generation due to landslide. Two types of landslide models were studied to estimate the significant run-up wave height on the southern shore of Hading Bay. **HAMPTOM (1972)** discussed that a submarine landslide has three stages of flow; landslide flow, subaqueous debris flow and turbidity-current flow. **JIANG & LeBLOND (1992)** have examined the coupled problem of underwater avalanches and the surface waves which they create and showed that less viscous material slides faster and causes larger waves. And **LeBOLD and JONES (1995)** suggested that underwater landslides of deformable sediments, that is corresponding to subaqueous debris flow and turbidity-current flow, have been relatively ineffective at generating sea surface waves as compared instantaneous displacement of the bottom to a configuration resulting from the effect of slide. Therefore, the model considered in this study takes into account only the first stage of the flow, that is landslide. The numerical simulation is carried out using the shallow water wave theory with drag force and mixing effect of the front of landslide. This would enable us to explain the cause of the significant difference of the run-up wave height between the northern and southern shores.

2. LANDSLIDE GENERATING MODELS

Several researchers have proposed several models for wave generation due to landslide. To name a few, **MING & WANG (1993)** developed two methods for the inflow process of the landslide in their study, that is: Inflow-Volume Method and Unit-Width-Discharge Method. **NODA (1970)** on the other hand developed two-dimensional box and a two-dimensional wall, the box is dropped vertically on the end of a semi-infinite channel for the method of vertical entry of land mass, and the wall which moves into the fluid domain for the horizontal entry. **JOHNSON & MADER (1994)** carried out the 1050 Ka Lanai tsunami, Hawaii, using the drop of assumed down and uplift area on the ocean floor as an initial condition.

Those methods used previously cannot be applied directly for the case of Flores tsunami due to the fact that higher tsunami heights were observed not on the opposite side of the landslide area but, along it

and its neighborhood. Thus, other types of models were developed for the case of the Flores Earthquake Tsunami by taking into account the kinematic and dynamic process of landslide near the coastal line. The models are shown in Figs. 4 - 6. The subsidence model (Model 1) is a simple model (Fig.4). The slope just drops vertically downward. In Fig. 4 the solid lines represent the initial slope with the dashed line as the new profile at each time step. The force causing the vertical drop is obtained as follows:

$$m\frac{d^2\xi}{dt^2} = g\left[1-(c+\tan\theta)\right] \qquad (1)$$

where m is the mass of soil, $\xi$the displacement of sea bottom/slope, c soil cohesiveness, and $tan\theta$ is the soil friction. Generally speaking, it is very difficult to estimate the time to stop the motion. It is supposed that the c become significantly small during a strong ground quake but it would return to be large after it then the motion will be terminated. The information of duration of ground quake is not available. For simplification, therefore, we assumed that the movement will cease when it reaches a pre-determined vertical displacement.

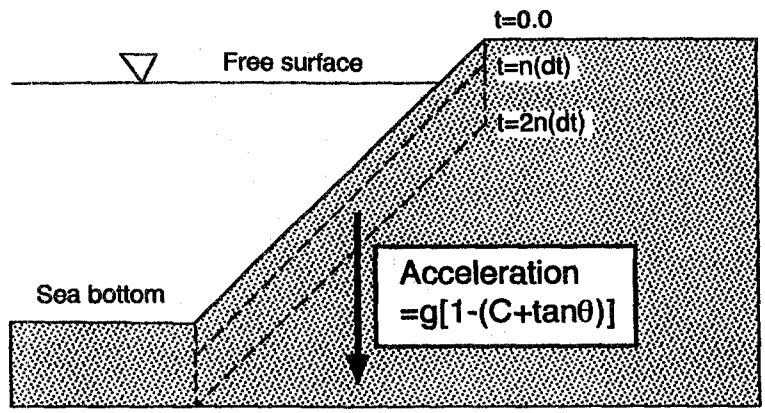

FIGURE 4 Subsidence model (Model 1), in which a slope drops vertically downward. C is the soil cohesiveness and $tan\theta$ is the soil friction.

In the second model, circular-arc model, two types of slip are considered; toe-slip (Model 2) and base-slip model (Model 3) as shown in Fig.5, which is similar to **OKUSA & YOSHIMA (1981)** model under the ocean. It is commonly assumed that the surface of failure for both type follows a circular arc profile, as can be seen in Fig.5. Movement is initiated when a sudden ground quake or external disturbance alters the balance of internal forces, the resisting force in the region-2 and the driving force in the region-1 shown in Fig.6, which are calculated by the balance between the friction and gravitational forces in the component of the slope at the each segment. Now, when this happens certain important properties of the soil suddenly alter its value, in this case the c and $tan\theta$ and if these

values are altered to such extent then it triggers a landslide

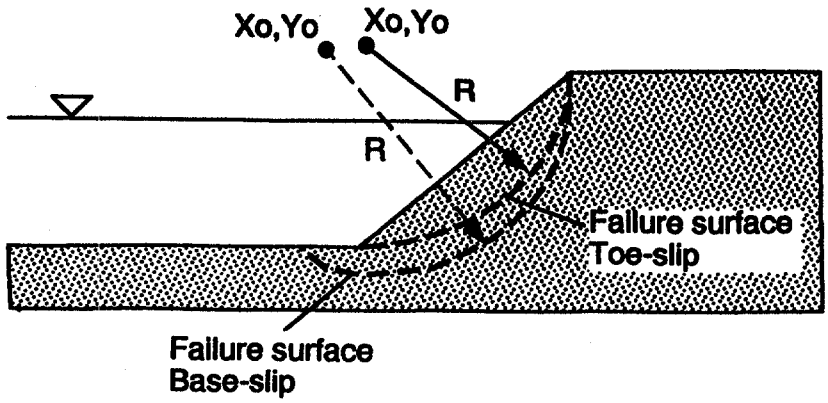

FIGURE 5 Circular-arc slip model ; toe-slip (Model-2) and base-slip (Model-3). The failure surface for both models is assumed to be circular arc profile.

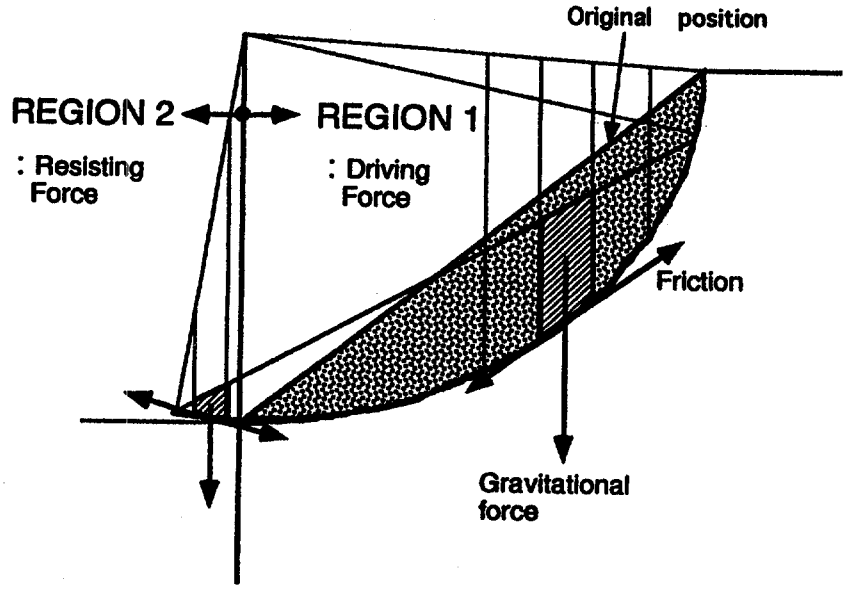

FIGURE 6 Movement of circular-arc slip model which is calculated by the balance between total driving force in Region -1 and total resisting one in Region-2.

3. WAVE GENERATION MODEL

The landslide model developed takes into account additional parameters like those for the sudden inflow of a certain volume due to landslide are drag effect at the front of the slide and bottom friction.

The mass conservation equation is:

$$\frac{\partial \eta}{\partial t} + \frac{\partial M}{\partial x} = \frac{\partial \xi}{\partial t} \qquad (2)$$

where η is the water surface, ξ the vertical displacement of sea bottom/slope, and M the discharge defined by

$$M = \int_{-h}^{\eta} u dz \qquad (3)$$

Parameters like the effect of drag and bottom friction used in this study are the same as those used by **RANEY and BUTLER(1976)**. Momentum equation is given as

$$\frac{\partial M}{\partial t} + \frac{\partial \left(\frac{M^2}{D}\right)}{\partial x} + gD\frac{\partial \eta}{\partial x} = R_x + L_x \qquad (4)$$

where$D$ is the total depth which is defined by

$$D = h + \eta \qquad (5)$$

and R_x is the bottom friction term, L_x is the drag effect of the front of slide

$$R_x = \frac{g\left(\frac{M}{D} - V\right)\left|\frac{M}{D} - V\right|}{C^2(h+\eta)} \qquad (6)$$

$$L_x = \frac{1}{2} C_D \frac{1}{h} \frac{A_z}{A_c}\left(\frac{M}{D} - V\right)\left|\frac{M}{D} - V\right| \qquad (7)$$

where A_Z is the vertical cross-sectional area (front of slide), C_D the drag force coefficient (front of slide),V the velocity of sea bottom displacement,C the chezy's roughness coefficient, A_c the grid cell area.

4. NUMERICAL METHOD

The non-linear basic governing equation of shallow water condition was solved numerically using the staggered leap-frog scheme. The computer program utilizes non-linear equations and computes

simultaneously the ground deformation due to landslide and the propagation of waves, which is due to ground deformation. Important terms in the momentum equation like drag and bottom friction are also computed.

A very common yet important parameter is found in both proposed models, that is, the acceleration of the land mass. Numerical scheme for acceleration was used in this study to calculate the next value of displacement. The standard numerical scheme of the basic second-order derivative equation for acceleration a, Eq. (8), is given in Eq. (9) :

$$a = \frac{d^2\xi}{dt^2} \qquad (8)$$

$$a = \frac{\xi_{n+1} - 2\xi_n + \xi_{n-1}}{\Delta t^2} \qquad (9)$$

Although the discretized difference equation, Eq. (9), is the higher order accurate scheme of the second order approximation, we have some inevitable change of numerical results depending the grid size, Δt, due to the disretization error including initial condition. The problem with the equation of Eq.(8) is called *an ill-posed problem* because the solution is strongly affected by the initial condition. Figures 7 and 8 show the example of this problem by using the following initial condition:

at t=0, ξ=0 and at t=Δt, ξ_1=0 (case-1 in Fig. 7)

at t=0, ξ=0 and at t=Δt, ξ_1=1.0 (case-2 in Fig. 8).

Both figures suggest the dependence of numerical results on the grid size, in which case-2 is more significant than case-1. The numerical result of case-1 with the finer grid size is approaching to the analytical solution of Eq.(8) with the initial condition; ξ_0=0 and $d\xi_0/dt$=0, while those of case-2 with the finer grid is divergences as shown in Fig.8.

Through deriving the analytical solution of the discretized difference equation of Eq. (9), let us discuss the reason and try to overcome this problem. Since Eq.(9) is categorized into *the inhomogeneous equation* being composed of particular and general solutions. Assuming the following general initial condition:

at t=0, $\xi=\xi_0$ and at t=Δt, $\xi=\xi_1$ (10)

we obtain the solution of Eq.(9) ;

$$\xi_n = \frac{a}{2}(n\Delta t)^2 + (1-n)\xi_0 + n\xi_1 - \frac{a}{2}n(\Delta t)^2 \qquad (11)$$

The above equation clearly explains the characteristics of the results shown in Fig. 7 as well as Fig.8.

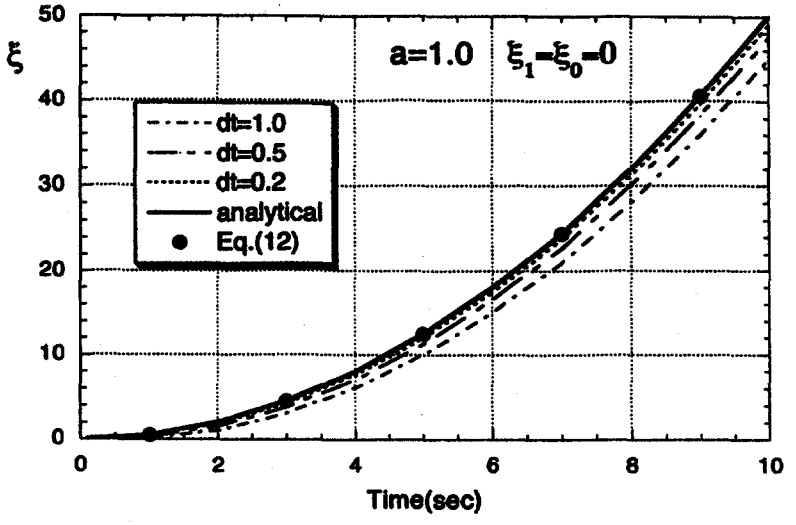

FIGURE 7 Calculation of the second-order derivative equations with different grid size, Δt. The computed result with a coarser grid is dissipated due to the discretization error.

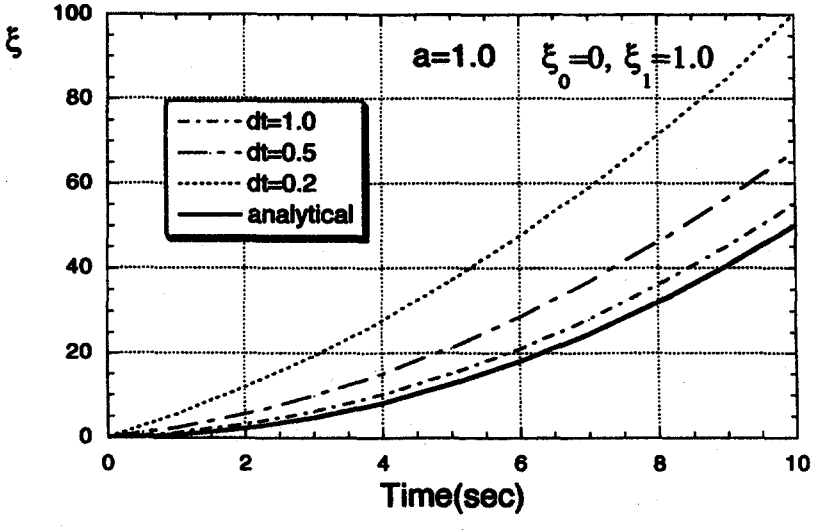

FIGURE 8 Calculation of the second-order derivative equation with the initial condition with $\xi_0=0$ and $\xi_1=1.0$.

In the case-1 with $\xi_0=0$ and $\xi_1=0$, the solution consists of only two terms; the first and the forth in the right side of Eq.(11), showing that the result with the coarser grid is dissipated due to the forth term (the discretization error). And in the case-2 with $\xi_0=0$ and $\xi_1=1.0$, the third term in Eq.(11) is added to the solution, which increases the numerical result inversely proportional to the grid size. Furthermore, it is interpreted that the numerical result with $\xi_0 \pi 0$ is to be decreased due to the second term in Eq.(11) with time.

The above discussion indicates that we have to select very much carefully the initial condition for the *ill-posed problem.* In order to avoid this problem, one of methods for the case of with $\xi_0=0$ and $\xi_1=0$ is proposed as follows:

$$\Delta\xi = \xi_n - \xi_{n-1} = a\Delta t\left[t+\frac{1}{2}\Delta t\right] \qquad (12)$$

As long as the value of the previous time step, ξ_n, is stored, a new value, ξ_{n+1}, is easily calculated using Eq.(12). This method shows perfect agreement with the analytical solution as shown in Fig.7 and is not affected by the position of initial condition of ξ_1, because the above equation is derived by connecting the analytical solution at each discretized region. However, it is not applied to the other case of $\xi_1 \neq 0$.

5. NUMERICAL RESULT

Geometrical condition and parameters in the simulation

The only available data for this research is the tsunami run-up wave heights while the exact or approximate value of the C and $tan\theta$ are unknown. Therefore, in order to simulate the wave generation due to landslide triggered by the Flores earthquake, the values of C and $\tan\theta$ are assumed in all three models as 0.1 kg/m^2 which would be expected to be the value during a strong ground quake. The pre-determined vertical displacement used for the subsidence model is 15.5 m. Taking into account the photos and witnesses' report in Flores Island [**TSUJI et al.(1995) and YEH et al.(1993)**], the radius of the circular arc failure for the circular-arc slip model is

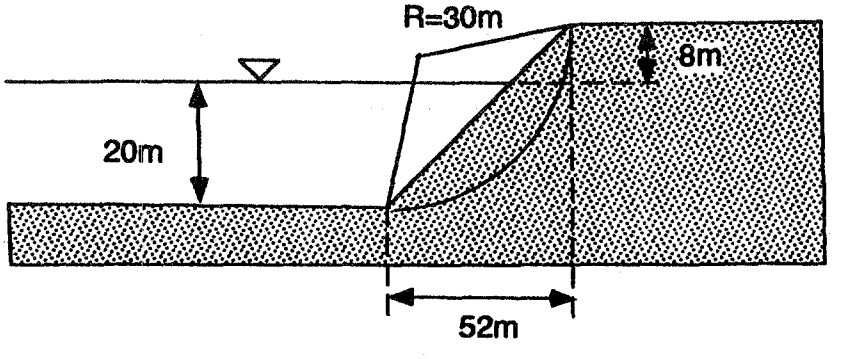

FIGURE 9 Geometrical condition for computation.

assumed to be 30 m for the toe-slip model, whereby the arc passes through the top and bottom edge of the slope while 42 m is used for the base slip model, whose arc passes through at 5 m inland from the

top edge of the slope and 20 m off-shore from the base of the slope. An initial water depth of 20 m is also assumed. The elevation of top edge was assumed at 8 m above the still water level and with 30° slope of the shoreline according to the photos taken in the Hading Bay. The above geometrical conditions are summarized in Fig.9.

Landslide simulation

The numerical simulation for displacement of the sea bottom is then conducted for all three models as shown in Figs.10-12. Regarding the effect of mixing or turbulence at the front of landslide under the sea, the diffusion is included specially for Model-3,because the result shows the unrealistic features such as discontinuity of slope and large amount mass at the front of landslide. Field data and reasonable physical explanation for them are not available. Thus, we estimate the approximate value of the coefficients through the simulation with different values of the coefficient. A result with the diffusion coefficient of 5.0 m^2/s (Fig.12) showed quite reasonable agreement. However, we remind that the further discussion on this value is required.

Wave Generation simulation

Since we are interested in the effect of the drag force, L_X, at the front of landslide shown in Eq.(7) in a wave generation, the simulation with and without the drag forces are carried out. It can be seen from the results that the effect of drag force does not affect the tsunami run-up wave height, suggesting that its effect in a relative deep sea would be small while it would be only dominant around the front. And the simulation with large coefficient of C_D causes the small disturbances on the surface. Therefore, the drag force in the present model is neglected.

Numerical results of the generated waves for each type of sea bottom deformation, Models 1-3, are shown in Figs.13-15 respectively. And in Fig.16, the plot shows the tsunami run-up wave height generated by each model. It is very clear that the subsidence model's (Model 1) run-up wave is not as high as that of the circular-arc slip model (Models 2 and 3). Even through we assume the large pre-determined displacement due to a landslide, the computed result might be still small. We can conclude that the circular-arc slip model is more appropriate in describing the significant phenomena in the southern shore of Hading Bay, as compared with the subsidence model.

6. CONCLUSIONS

Although numerous researches on landslide generated waves have already been done the developed models cannot be applied for our study in the southern shore of Hading Bay, because these models do not include the movement of the landslide. Thus, two types of model are proposed: Circular-arc slip model and subsidence model, which also includes the kinematic and dynamic process of the landslide near the coastal line. Numerical scheme to calculate a sea slope deformation is proposed. The solution of the proposed scheme showed a perfect fit with the analytical solution Thus, the proposed numerical scheme for acceleration (Eq. 12) is used in this study.

The comparison of the simulations with three models suggests that the most appropriate one is circular-arc slip model, as far as a tsunami run-up. Yet, there are two models in this category; toe-slip model (Model 2) and base slip model (Model 3). Although it was seen in Fig. 16 that the run-up wave height of Model 3 is better than Model 2, we cannot immediately select Model 3 as the most appropriate model of the two. The selection between Models 2 and 3 awaits confirmation on further detailed data on a site of Flores Island, Indonesia.

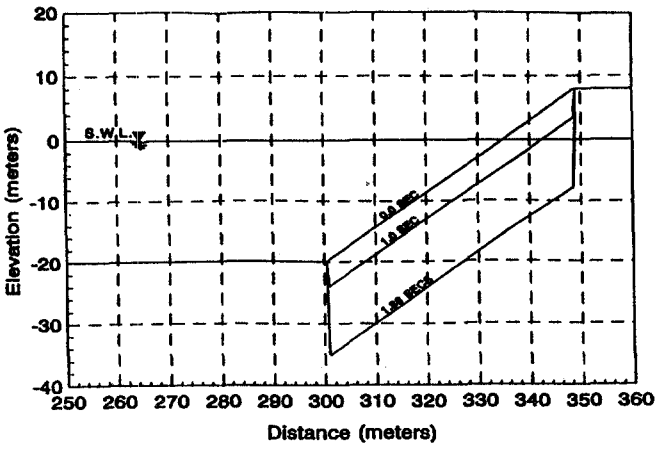

FIGURE 10 Computed displacement of the sea bottom by Model-1.

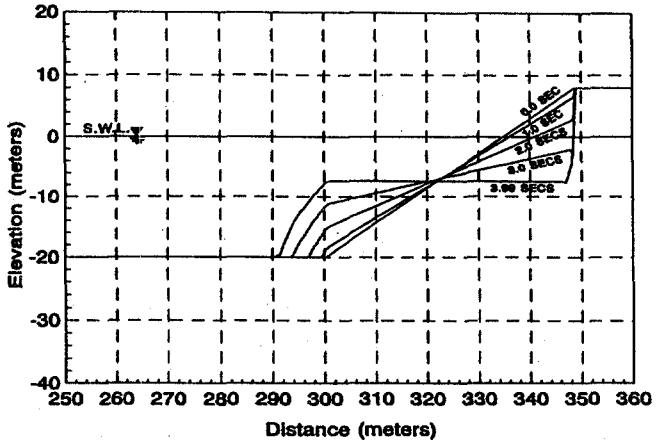

FIGURE 11 Computed displacement of the sea bottom by Model-2.

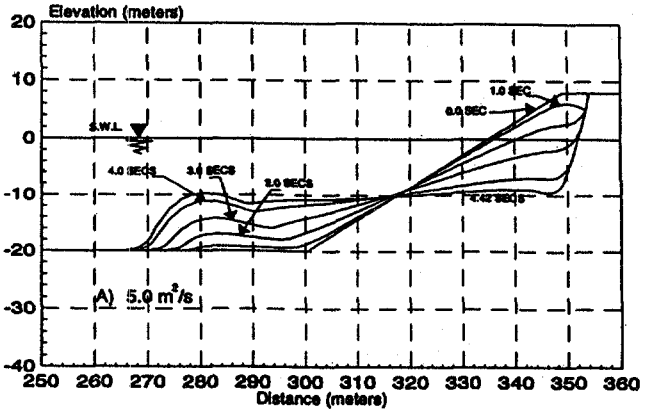

FIGURE 12 Computed displacement of the sea bottom by Model-3.

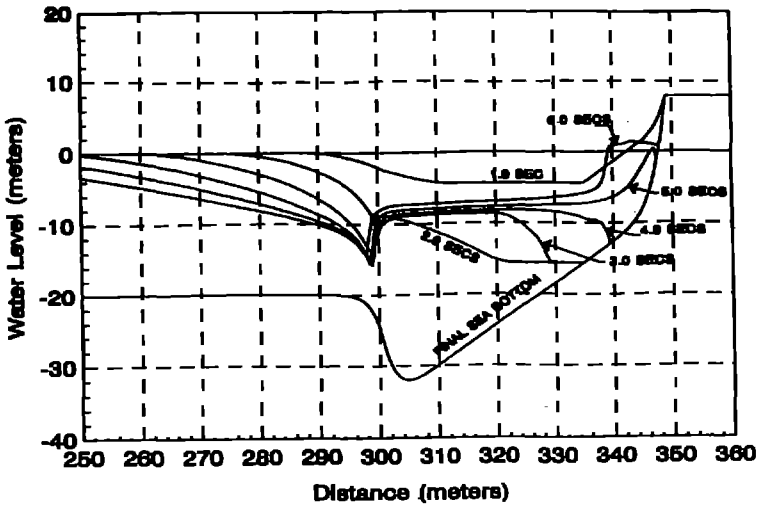

FIGURE 13 Computed wave profiles by Model-1.

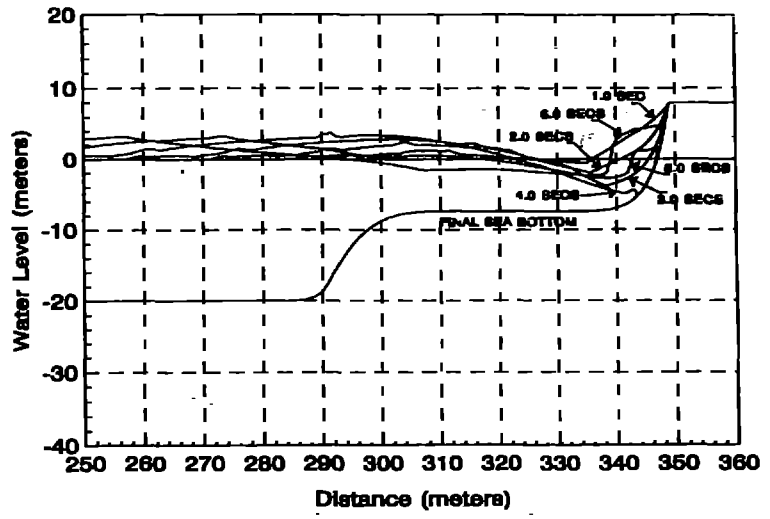

FIGURE 14 Computed wave profiles by Model-2.

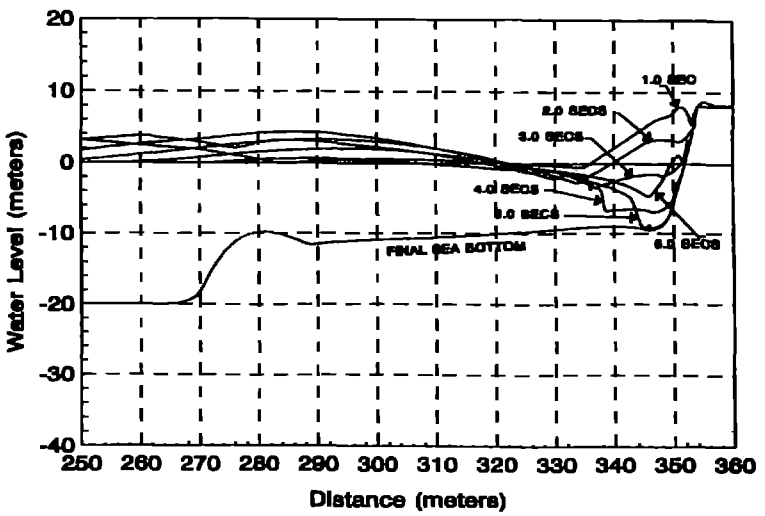

FIGURE 15 Computed wave profiles by Model-3.

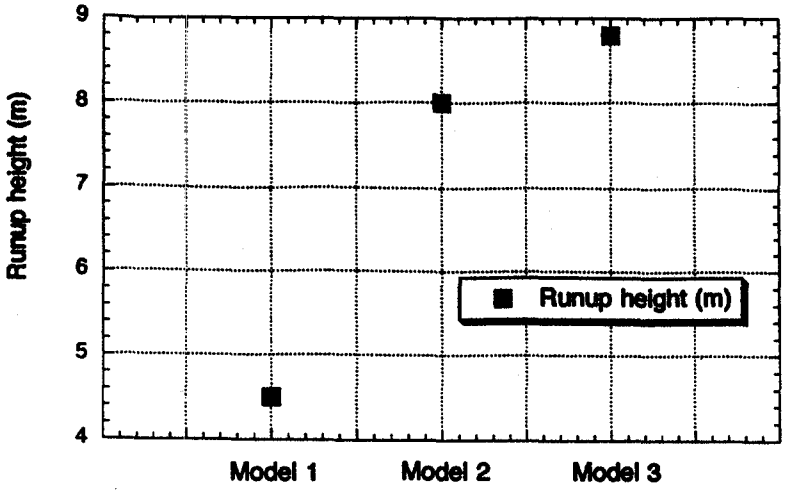

FIGURE 16 Comparison of computed run-up heights among three models.

ACKNOWLEDGEMENT

We wish to express our thanks to Dr. Harumichi Kyotoh, Asian Institute of Technology for his suggestion on the numerical method. This study was partially supported by co-operative research grant from the Ministry of Education, Science and Culture, Japan (0604405), and the publication is financially supported by the Ogawa Commemoration Fund.

REFERENCES

AIDA,I. (1974)"*Numerical Computation of a Tsunami Based on a Fault Origin Model of an Earthquake*", JISIN 2nd series, Journal of Seism.Soc.Japan, Vol.27, pp.141-154, (in Japanese).

HAMPTON, M. A.(1972) *"The Role of Subaqueous Debris Flow in Generating Turbidity Currents "*, Journal of Sedimentary Petrology, Vol. 42, No. 4, December 1972, pp. 775-793.

HUNT B.(1988)*"Water Waves Generated by Distant Landslide"*, Journal of Hydraulic Research, Vol. 26, No. 3, 1988.

IMAMURA, F. and KIKUCHI, M (1994) *"Moment Release of the 1992 Flores Island Earthquake Inferred from Tsunami and Teleseismic Data"*, Science of Tsunami Hazards, Vol.12, No.2, pp.67-76,1994.

IMAMURA,F.(1995), *"Review of Tsunami Simulation with a Finite Difference Method"*, Int.Long Wave Runup Workshop, Friday harbor, Washington, US, 30p..

JIANG, L. and LeBOLD, P.H.(1993), *"The coupling of a submarine slide and the surface waves which it generates"*, J.Geo.Res., Vol.98, pp.10,303-10,317.

JOHNSON, C. and Charles L. MADER,C.L. (1994)," *Modeling the 105 Ka Lanai Tsunami*", Science of Tsunami Hazards, Vol.12, pp.33-36.

LeBOLD,P.H. and JONES,A.T.(1995), "*Underwater Landslides ineffective at Tsunami Generation*", Science of Tsunami Hazards, Vol.13, No.1, pp.25-26.

MING D., and WANG, D.(1993)*"Studies on Waves Generated by Landslide"*, Proceedings of XXV Congress of IAHR, Technical Session C, pp. 1-8.

NODA, E.K.(1970) *"Water Waves Generated by Landslides"*, Journal of Waterways, Harbors and Coastal Engineering Division, ASCE, Vol. 96, No. WW4, Proceeding paper 7699, pp. 835-855.

OKUSA,S. and M.YOSHIMURA (1981), "*Possibility of Submarine Slope Failure Due To Waves*", Tokai University Bulletin, Vol.14, pp.227-234, (in Japanese).

RANEY, D.C. and BUTLER, H.L.(1976)*"Landslide Generated Water Wave Model"*, Journal of Hydraulic Division, ASCE, Vol. 102, No. HY9.

TSUJI Y. et al. (1995):"*Damage of coastal villages due to the 1992 Flores Island earthquake tsunami*", Topical issue of Tsunami 1992-94, Pure and Applied Geophysics, Vol.144, No.3/4.

YEH, H., IMAMURA, F., SYONOLAKIS, C., TSUJI, Y., LIU, P. SHI, S.,; *"The Flores Island Tsunamis", Eos*, American Geophysical Union, Transactions, Vol. 74, No. 33, 17 August 1993, pp. 369-373.

ON SOME PROPERTIES OF THE FE TSUNAMI "WAVE PROPAGATOR"

Stefano Tinti, Alessio Piatanesi and Elisabetta Bortolucci

**Università di Bologna, Dipartimento di Fisica,
Settore di Geofisica, Viale Berti Pichat, 8
40127 Bologna, Italy.**

ABSTRACT

The concept of wave propagator in Finite-Element (FE) tsunami modeling was first introduced in a previous paper (Tinti and Piatanesi, 1995), where it was shown that, in the framework of the linear theory, tsunami evolution can be computed by simply applying a linear operator, that was called "wave propagator", to the initial source field (water elevation and velocity). The wave propagator is uniquely identified by its spectral characteristics, that is by its set of eigenvectors and eigenvalues, respectively related to space and to time wave evolution. The solution at any time can be seen as resulting from superposing the eigenvectors according to a weighing scheme depending on the initial field. In this paper we will illustrate some properties of the wave propagator spectrum, particularly focussing our attention on the dependence of eigenvectors and eigenvalues from the geometrical characteristics of the FE grid. It is found that the eigenvalues are invariant under a certain class of transformation (grid rotation, scaling of variables). It is further found that the maximum eigenvalues is related to the minimum crossing time, i.e. the minimum time taken by a wave to cross a grid element.

Finite-Element modeling of wave propagation in a finite basin entails the partition of the basin into an N-node grid and the description of the hydrodynamic fields by means of N-component time dependent vectors. Let us denote by $\zeta(t), u(t)$ and $v(t)$ the vectors representing the sea water elevation above the mean sea level and the horizontal components of the water velocity, and let us further designate by $\xi(t)$ the $3N$-component vector defined by:

$$\xi(t) = \begin{pmatrix} \zeta(t) \\ u(t) \\ v(t) \end{pmatrix} \tag{1}$$

In the linear shallow water approximation, that is often advantageously used in modelling tsunamis (see e.g. Satake, 1995), wave evolution is governed by a set of differential equations that involves the above field vectors and that can be given the basic form (Tinti and Piatanesi, 1995):

$$\begin{cases} \dot{\xi}(t) = C\xi(t) \\ \xi(0) = \xi_0 \end{cases} \tag{2}$$

where C is a $3N$ by $3N$ constant real matrix and ξ_0 is the vector representing the initial condition at time $t = 0$, and the dot stands for the total time derivation. Basing on the theory of linear first-order differential systems, the solution to the problem (2) can be given the expression:

$$\xi(t) = P(t)\ \xi_0, \qquad P(t) = Ee^{\Lambda t}E^{-1} \tag{3}$$

where E and Λ are respectively the eigenvector and the eigenvalue matrices associated with C: this means that the columns of E are the unit eigenvectors of C, forming a complete, not necessarily orthonormal basis in the $3N$ vector space, while Λ is a diagonal matrix formed by the eigenvalues of C. This can be formally stated by means of the factorization $C = E\Lambda E^{-1}$, that can be referred to as the spectral decomposition of C. Consider that C being real implies that $P(t)$ is real as well, though generally E and Λ are complex matrices. The real operator $P(t)$ defined in the eq.(3) was called wave propagator since it fully describes the evolution of the waves from a given initial perturbation. The main difference between the method based on the wave propagator and the traditional FE techniques is that the latter compute the evolving solution step by step (computing the solution at time t imposes the computation at all intermediate times $t_i = i\Delta T, i = 1, 2, ...m, m = t/\Delta T$, where ΔT is the allowed time step), whereas the former is able to provide the solution at any time directly. Furthermore, it is remarked that the above expression holds even when linear boundary conditions are

added to the problem, provided that the matrix C be replaced by the matrix VC, where V is the so-called bounding operator (Tinti and Piatanesi, 1995), that is a matrix transforming a generic vector ξ into a vector $\xi' = V\xi$ satisfying the conditions on the grid boundaries. One interesting property of the eigenvectors of VC is that they all respect the boundary conditions. This generalization is of fundamental value, since it allows to use the above theory extensively in practical applications where, as is known, boundary conditions are to be always specified. The eq.(3) suggests the interpretation of the wave propagator $P(t)$ as a multiple operator consisting of three consecutive transformations: 1) projection of ξ_0 into the space of the eigenvectors providing its spectral components (E^{-1}); 2) evolution in time of each single component ($\exp(\Lambda t)$); 3) final synthesis of all the components (E). It is further observed that the complex eigenvectors can be seen as grid eigenmodes: given an N-node mesh, there are $3N$ independent eigenvectors whose various combinations render all possible solutions the model can describe. In the following sections we will illustrate further the meaning of the eigenmodes and subsequently study the dependence of the spectral decomposition of the wave propagator upon the geometrical features of the grid, which is the main goal of this paper.

ROTATION AND SCALING

Physical principles require that the solution to any physical problem be invariant under rotation of the coordinates system: this implies that if we rotate the computational grid by an angle α, and we likewisely rotate the initial horizontal velocity fields $u(0)$ and $v(0)$, we expect to obtain a solution with unchanged elevation and with rotated velocities. In order to explore how a coordinate rotation affects the wave propagator, let us proceed through a formal approach. In the $3N$ vector space swept by ξ a geometrical rotation corresponds to a real $3N$ by $3N$ matrix R mapping $\xi = (\zeta, u, v)$ to its image $\xi' = (\zeta', u', v')$. The matrix R is a block matrix consisting of 9 N by N blocks: $R_{z'z}, R_{z'u}, R_{z'v}$, etc. The water elevation remaining unchanged under rotation implies that $R_{z'z} = I_N$, that is the identity matrix in the N-dimension space, and that $R_{z'u} = R_{z'v} = 0$. As to the velocity fields, if we notice that at the node j the components of the new velocity u'_j and v'_j depend only on the corresponding components u_j and v_j, it is straightforward to conclude that $R_{u'z} = R_{v'z} = 0$ and that $R_{u'u} = R_{v'v} = I_N \cos\alpha$, $R_{u'v} = -R_{v'u} = I_N \sin\alpha$, α being the amplitude of counterclockwise rotation. It is then easy to prove that $R(\alpha)$ (we make explicit the dependence upon the angle) is a rotation operator in the 3N vector space and that $R(\alpha)^{-1} = R(\alpha)^T = R(-\alpha)$. With the foregoing in mind, we are now able to examine the effect of the rotation on the wave propagator. After left-multiplication by R, the system (2) becomes:

$$\begin{cases} R\dot{\xi}(t) = RCR^{-1}R\xi(t) \\ R\xi(0) = R\xi_0 \end{cases} \tag{4}$$

and after introducing the rotated vector $\xi' = R\xi$, it can be given the same form as in the set (2), provided that ξ be replaced by ξ' and that C be substituted by $C' = RCR^{-1}$. Accordingly, after spectrally decomposing C' as $C' = E'\Lambda' E'^{-1}$, the solution (3) can be deduced in terms of the wave operator $P'(t)$. The question to pose now regards the relationship between E' and E, and between Λ' and Λ. In order to provide an answer, we first observe that C' can be easily written as:

$$C' = RCR^{-1} = R(E\Lambda E^{-1})R^{-1} = (RE)\Lambda(RE)^{-1} \tag{5}$$

Hence, after comparing the last expression in the above chain of equations to the spectral decomposition of C', we could infer that

$$E' = RE \qquad \Lambda' = \Lambda \tag{6}$$

only if RE is proven to be an eigenvector matrix, that is a matrix of rank $3N$ whose columns are unit $3N$ vectors. But this point is immediate to demonstrate, given that E' is the image of the eigenvector matrix E under the rotation R and that any rotation cannot change the norm of a vector. Therefore, looking at the eqs.(6), the basic conclusion to draw is that a geometric rotation of the grid has the simple effect of rotating likewisely the eigenvectors of the problem, but it leaves unchanged the corresponding eigenvalues.

Scaling is a mathematical transformation whereby dimensional physical quantities appearing in differential equations are made dimensionless in a suitable way. In our case, the vector $\xi(t)$ defined by eq.(1) is easily verified to have heterogeneous components, for its first N components are lenghts, while the other $2N$ are velocities. Accordingly, the basic matrix C is likewisely formed by heterogeneous elements. So, if the dynamic fields at the node j, that is $\zeta_j(t)$, $u_j(t)$ and $v_j(t)$ are divided by the respective characteristic values ζ_j^*, u_j^* and v_j^*, the resulting components at that node will be all dimensionless. In the $3N$ vector space, the above process is realized by introducing the scaling operator S that is a real diagonal matrix formed by the inverse of the typical elevations and velocities at each single node, and by applying it to $\xi(t)$:

$$\xi'(t) = S\xi(t) \tag{7}$$

It is clear that $\xi'(t)$ is a dimensionless vector, and, moreover, that its components turn out to be balanced, i.e. to have the same order of magnitude, if the scaling values are chosen in a clever way. Following a line analogous to that we used when we dealt with rotations, we can arrive again at the system (4), where S is now meant to be replacing R. Let us then define the dimensionless time $t' = t/\tau$, where τ is a characteristic propagation time interval, and let us consequently write the time derivative $\mathrm{d}/\mathrm{d}t'$ as $\tau\mathrm{d}/\mathrm{d}t$. Hence the system (4) transforms to:

$$\begin{cases} S\dot{\xi}(t) = C'\xi(t) \qquad C' = \tau SCS^{-1}R \\ S\xi(0) = S\xi_0 \end{cases} \tag{8}$$

where the dot now denotes differentiating with respect to t'. It is easy to recognize that the above factorization of C', implying that $C' = (SE)\tau\Lambda(SE)^{-1}$, is not the spectral decomposition of $C' = E'\Lambda'E'^{-1}$, because the columns of SE are not unit vectors, owing to S not being in general a unitary matrix. But in order to normalize the columns of a given matrix, say M, we can always use a diagonal normalizing operator whose j-th diagonal element is the inverse of the norm of the j-th column of M. If we designate by N_E such a normalizing operator in our case, we conclude that:

$$C' = (SE)(N_E N_E^{-1})\tau\Lambda(N_E N_E^{-1})(SE)^{-1} = (SEN_E)\tau\Lambda(SEN_E)^{-1} \qquad (9)$$

where advantage has been taken from the fact that Λ and N_E commute being diagonal matrices. The above factorization allows us to state that:

$$E' = SEN_E \qquad \Lambda' = \tau\Lambda \qquad (10)$$

which implies that the scaled wave propagator P' is a propagator having eigenvectors that can be obtained from the eigenvectors of P through scaling and normalization, and similarly having eigenvalues that can be computed by scaling the eigenvalues of P.
In order to illustrate the above properties we will make recourse to the numerical example of a basin consisting in a rectangular channel, a case so simple that is perfectly adequate for numerical tests (Tinti and Gavagni, 1995; Tinti and Piatanesi, 1995). The mesh is formed by 168 equal triangles corresponding to 105 nodes, the basin length and width being respectively 11,550 m (along the x-axis) and 5,775 m (along the y-axis). The origin of the (x,y) plane coincides with the left right corner of the channel. After applying the FE discretizing technique fully described elsewhere (Tinti et al., 1994), the matrix C of system (4) is computed along with its spectral decomposition. Figure 1 shows its $3N = 315$ eigenvalues in decreasing order of magnitude for a grid rotated counterclockwisely by an angle $\alpha = 30°$. The eigenvalues are scaled through the minimum time τ that is taken by a water wave to cross a grid element. At the moment we stress two points: 1) the maximum eigenvalue exceeds slightly unit, meaning that the highest frequency that can be propagated across the grid is of order τ^{-1}; 2) the eigenvalues norm curve (upper panel) can be divided in two ranges: it shows first a gently decreasing slope (range 1: from eigenvalue 1-205), followed by a drastic fall to eigenvalues some order of magnitude smaller (range 2: eigenvalues 206-315) We tested several grids corresponding to different rotations and we found exactly the same eigenvalues in the range 1, but different, though always very small, values in the range 2. This has a simple explanation, in that all eigenvalues in the range 2 should be vanishing, but owing to numerical errors affecting computations in a different way in different cases, they come out to be "quasi-zero", but differing from each other. From a physical viewpoint, zero eigenvalues correspond to a part of the spectrum associated with a steady state that is independent from time (see eq.(3)), and that can be accordingly neglected, since it plays no role in wave propagation across open basins. The spectrum of Figure 1 was actually computed for a flat 5 m deep basin, but in virtue of the scaling

through τ and in force of the theory illustrated above, it refers to flat basins of any depth. In general we can state that, if we compute the τ-scaled eigenvalue spectrum for a given mesh and bathymetry h_j $(j = 1, 2, ..., N)$, the same spectrum applies for the entire class of basins with the same mesh and a proportional bathymetry $(h'_j = kh_j)$, provided that the scaling time be chosen in such a way that $\tau' = \tau/\sqrt{k}$.

Spectral Dependence on the Basin Depth

At the end of the previous section we have mentioned the invariance of the spectrum for special transformation of the basin bathymetry. Here we will address how the spectrum is affected if the basin depth is changed in a more general way. To this purpose, let us take into account the previous rectangular channel and assume that it is transversally homogenenous, having however the depth h_1 and h_2 at the respective left and right end, being $h_1 < h_2$. We will examine the cases where: 1) the bathymetry changes linearly from h_1 to h_2; 2) the depth is h_1 (shallower waters) up to a given position at a certain distance from the left end, and then it changes abruptly to the value h_2 (deeper waters). Varying the position of the depth discontinuity, different bathymetries are obtained. Figure 2 refers to the case where the depth jump is in the middle of the basin and shows a typical eigenvector, whose structure is visibly influenced strongly by the depth jump. Figure 3 shows together the absolute value curves of eigenvalues referring to different bathymetries (flat bottom, shallow-deep water discontinuity at 1/2, 3/4, and 7/8 of the channel length, linearly changing depth) and gives us the opportunity to make some observations. First of all we premise that we will assume a floor step that is extreme and certainly unsuitable for shallow water approximation, but that, giving exaggerated effects, serves quite effectively to the purpose of illustrating clearly the action of a variable bathymetry on the eigenvalues structure. Examining Figure 3, let us consider the two eigenvalue curves related to flat bottoms as reference curves: curve 1 and curve 2 referring to the respective depth $h_1 = 1$m and $h_2 = 100$m. Notice that, as expected from the aforegoing discussion, the ratio r between corresponding eigenvalues is constant. Indeed, after posing $\tau_k = L/\sqrt{gh_k}k = 1, 2$ where L is a characteristic grid element length and g the acceleration of gravity, in virtue of the invariance law of the scaled eigenvalues we can state that $\tau_2\lambda_{2,i} = (\tau_1\lambda_{1,i})$, wherefrom we deduce that $r = |\lambda_{2,i}|/|\lambda_{1,i}| = \sqrt{h_2/h_1}$. Since in our case $r = 10$, curve 1 lies below curve 2 in Figure 3, the values of the former being constantly one tenth of the corresponding values of the other. Consider now the curves refferring to the floor step: it is seen that they tend to overlap the curve 1 ($h_1 = 1$ m), and that the entity of the overlapping increases along with the length of the channel with shallower waters. More explicitly, the channel having 7/8 of its length at the depth $h_1 = 1$ m and 1/8 at the depth $h_2 = 100$ m shares most of its low-frequency eigenvalues with the flat 1 m deep channel (eigenvalues 41-205), while correspondingly the highest frequency spectrum (1-40) has a smaller band, and starting

equally from a value close to unit, is steeper. Analogous effect can be observed for the other two step-related curves, with the common low-frequency spectral band getting narrower as the shallow part of the channel is made shorter. Interestingly, on the other hand, the curve corresponding to the linearly changing bathymetry exhibits a spectrum decreasing gradually from curve 2 to curve 1, which means that all eigenvalues result to be affected in this case.

Conclusions

In this paper we have elucidated some properties of the wave propagator spectrum that were not inspected in the paper were it was first introduced (Tinti and Piatanesi, 1995) for tsunami modeling. The paper has a prevailing theoretical approach exhibiting propension for mathematical rigour and clearness, but it does not forget to illustrate the physical implications of such properties for the wave propagation. The idea entailed by the wave propagator that the solution to the tsunami problem be a suitable synthesis of eigenmodes determined by the finite-element grid is promising and we believed that in the future it could be used in practical tsunami simulations. This justifies our efforts in trying to explore in great detail all the properties of its spectrum, and most importantly its relationship with the geometrical characteristics of the grid. Here we have exhaustively studied two kinds of tranformation, that is grid rotation and variable scaling, and have furthermore investigated some effects of the bathymetry on the eigenvalue structure.

Acknowledgments

This research was supported partly by the "Consiglio Nazionale delle Ricerche" (CNR) and partly by the "Ministero dell' Università e della Ricerca Scientifica e Tecnologica" (MURST). This research made use also of European Union funds.

References

Satake K., 1995, Linear and nonlinear computations of the 1992 Nicaragua earthquake tsunami, Pure and Applied Geophysics, 144, 455-470.

Tinti S. and Gavagni I., 1995. A smoothing algorithm to enhance Finite-Element modeling: an application to the 5 February 1783 Calabrian case, Italy, *Natural Hazards*, 12, 161-197.

Tinti S., Gavagni I. and Piatanesi A., 1994. A finite-element numerical approach for modeling tsunamis, *Annali di Geofisica*, 37, 1009-1026.

Tinti S. and Piatanesi A., 1995, Wave propagator in finite-element modeling of tsunamis, *Marine Geodesy*, 18, (in press).

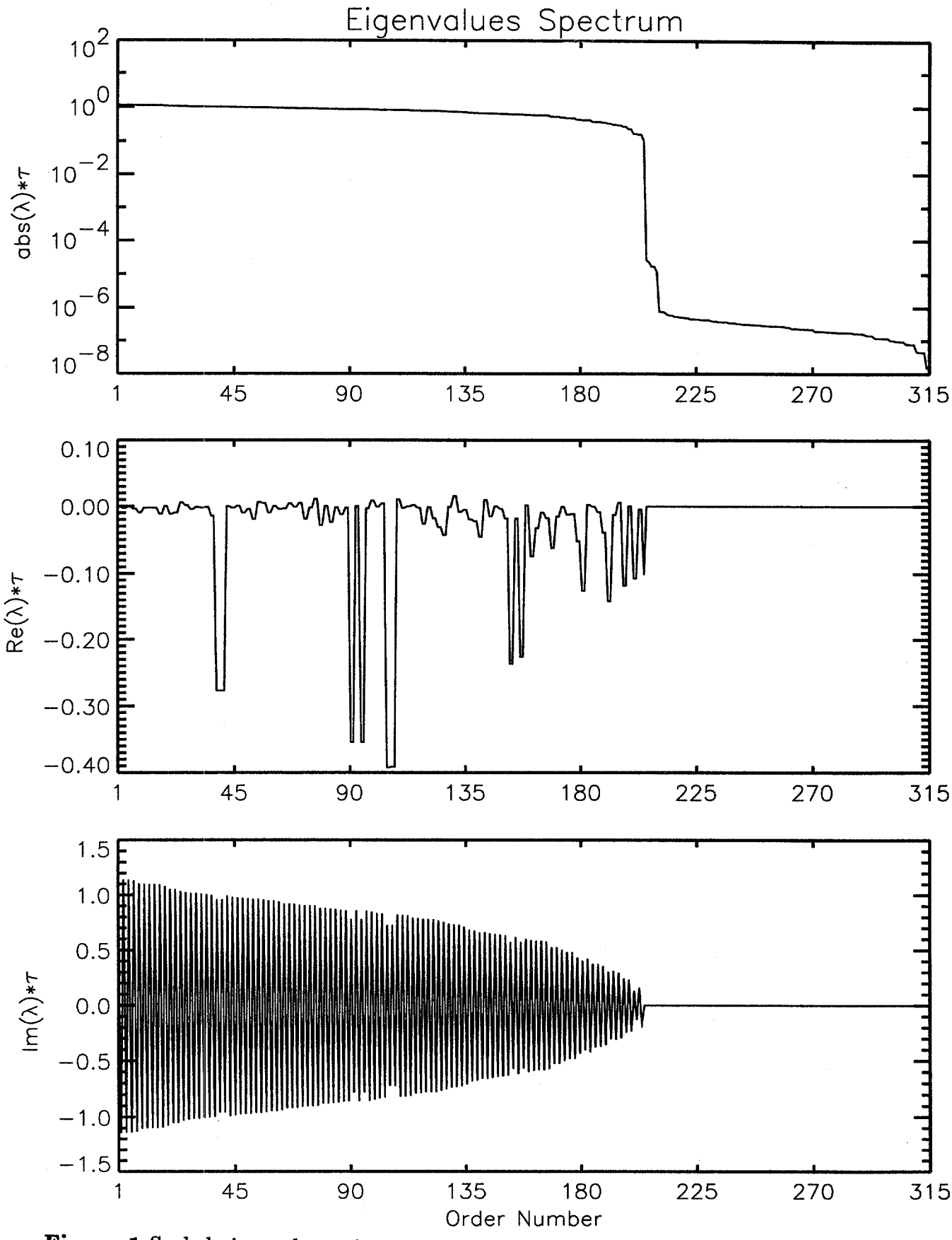

Figure 1 Scaled eigenvalues of a rectangular equal-triangle grid with $N = 105$ nodes. The grid corresponds to a flat bottom channel with longitudinal axis forming an angle $\alpha = 30°$ with respect the x-axis. Eigenvalues from 205-315 are numerical zeros. Of the complex eigenvalues the positive (negative) real parts determine an exponential growth (decay) of the corresponding grid eigenmode, while the imaginary part is associated to an oscillatory behaviour.

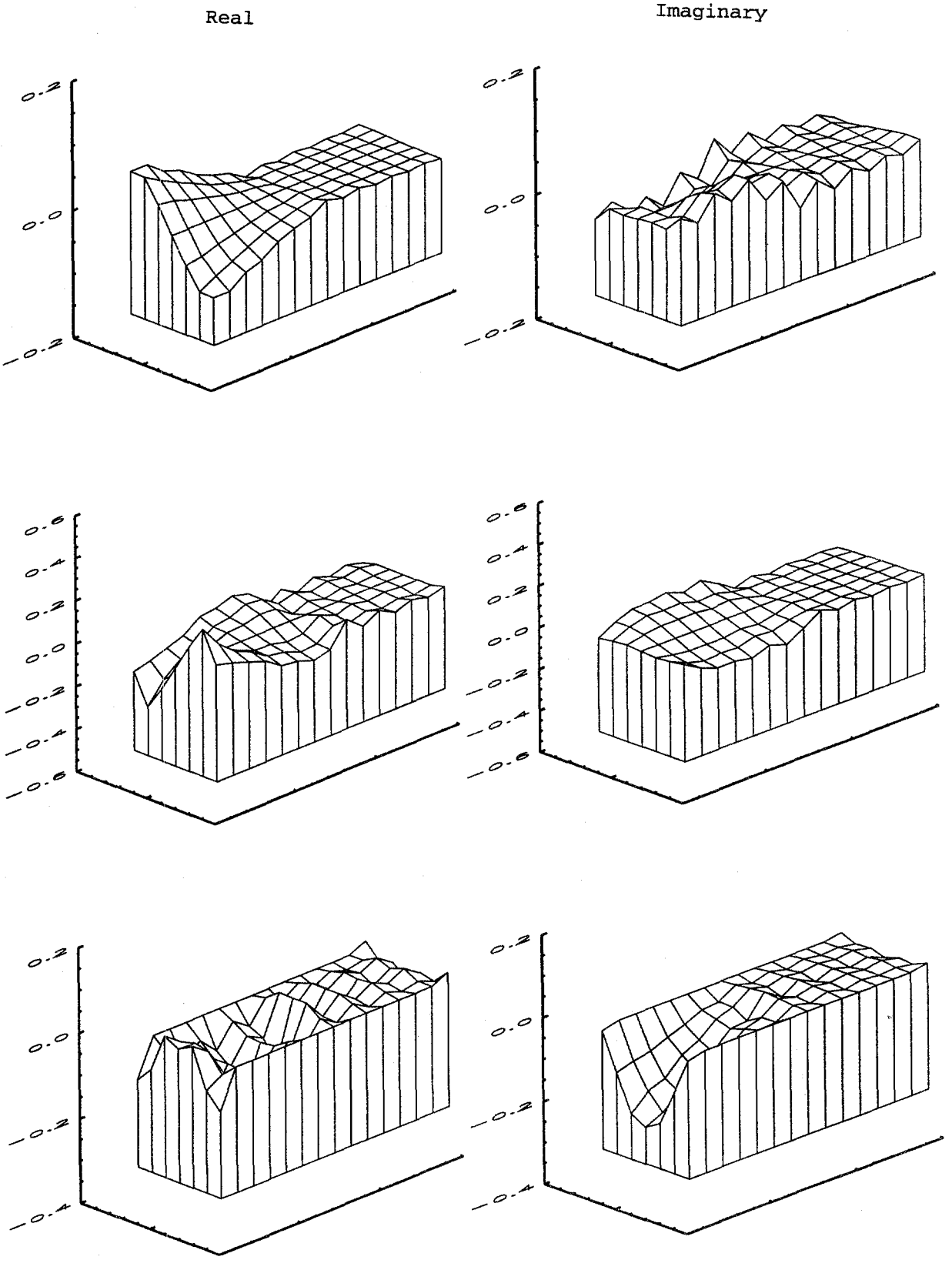

Figure 2 Real and imaginary parts of the low-frequency grid eigenmode 201 for a rectangular channel with an extreme depth discontinuity (1 m depth from one end to the middle, and 100 m depth in the remnant half). Each eigenvector describes completeley the elevation field as well as both velocity fields (longitudinal and transversal). The real and imaginary parts correspond to two physical states attained by the grid mode at two different times one quarth of a cycle apart.

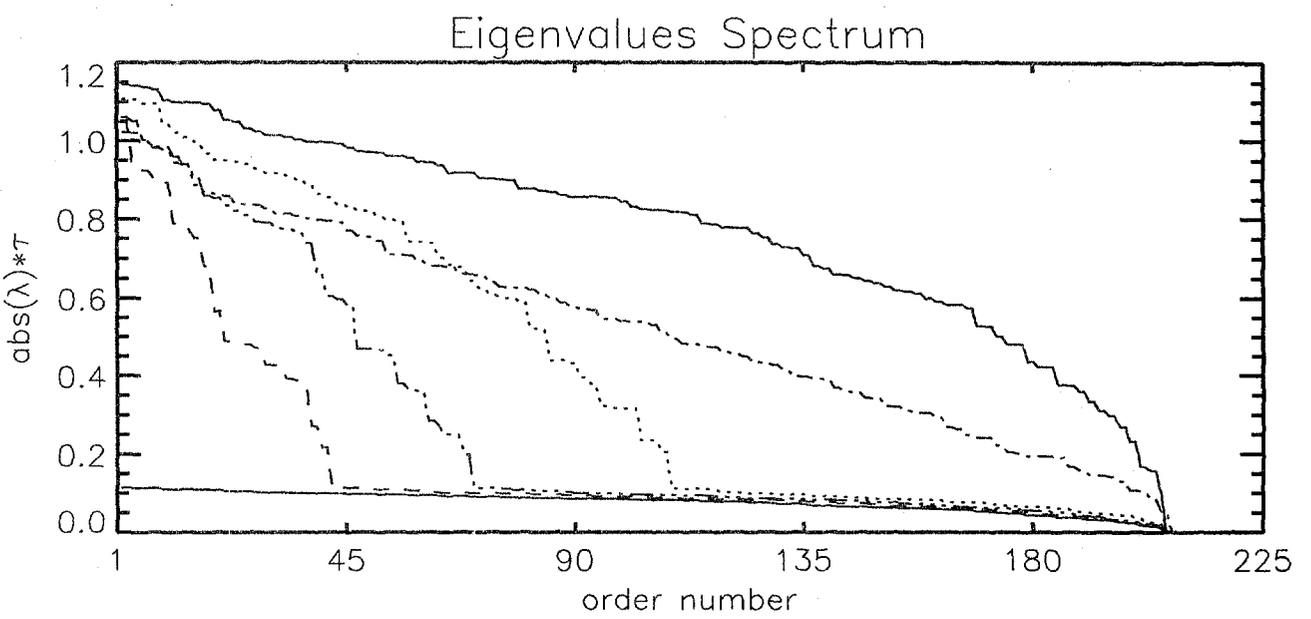

Figure 3 Scaled eigenvalues spectrum for different bathymetries. Upper solid curve: flat 100 m deep channel; lower solid curve: flat 1 m deep channel; dashed, dashed-triply dotted, dotted curves: stepped bottom channel with respective 7/8, 3/4 and 1/2 length at 1 m depth and the rest at 100 m depth; dashed-dotted curve: linearly changing bottom from 1 m at one channel end to 100 m at the other channel end. The time τ used for scaling refers to the deeper constant-depth channel.

EARTHQUAKES, TSUNAMIS, AND TECTONIC SETTING OF THE JAPAN TRENCH AND THE SOUTHWESTERN KURIL TRENCH AREAS

Ei-ichi Honza

Geological Survey of Japan.
Present Address: Geological Survey of Malaysia,
P O Box 1015, Jalan Sultan Azlan Shah 30820, Ipoh, Malaysia

Augustine S. Furumoto

Hawaii Institute of Geophysics and Planetology
University of Hawaii
Honolulu, Hawaii, 96822, U. S. A.

ABSTRACT

Between the years 1951 and 1995, the Japan Meteorological Agency (JMA) reported 20 shallow earthquakes ($h \leq 20$ km) of magnitudes $Ms \geq 6.2$ in the Tohoku forearc region, which is offshore from the Pacific Coast of northern Honshu Island, Japan. In spite of the fact that the region is a very active subduction zone, of the 20 large "shallow" earthquakes, only two generated tsunamis with run-ups higher than 1 m, nine generated minor tsunamis with run-ups less than 1 m, and nine did not generate any detectable tsunami.

When ocean bottom seismometer arrays were deployed in the region, for the same earthquakes, focal depths by ocean arrays yielded deeper values than focal depths by land-based arrays of the JMA.

Seismic profiling in the Tohoku forearc region detected numerous faults in the ocean bottom sediments, but the fault lengths were too short to have been associated with earthquakes of magnitudes greater than 6.2. Furthermore the faults in the sediments were usually confined to the Neogene sediments and did not penetrate to the Paleogene sediments.

The above evidences seem to indicate that focal depths of "shallow" earthquakes are actually deeper that reported by JMA. It is suggested that the discrepancy is due to the velocity structure used in source parameter determinations.

The deeper foci account for the fortunate dearth of damaging tsunamis in this active region.

Introduction

Earthquakes occurring in the Tohoku forearc region (eastern part from the volcanic chain of northern Honshu Island, Japan) are attributed to the subduction process of the Pacific lithospheric slab burrowing under the Japanese island arc. The subduction process gives rise to a two seismic zones, the upper zone along the upper slab boundary and the lower zone forming a layer along the middle of the slab. By far most of the earthquakes occur in the upper zone (e.g. Hasegawa et al., 1978; Yoshii, 1979). The shallow thrust zone (0-40 km) and the deep thrust zone (40-60km) occur along the upper seismic zone. The down-dip compression zone occurs along the upper seismic zone somewhat deeper than the aseismic front. The down-dip tension zone occurs approximately 20 km beneath the deeper thrust and down-dip compression zones (Umino and Hasegawa, 1982; Kawakatsu and Seno, 1983). Horizontal tension generated by bending of the oceanic plate occurs in the subducting oceanic slab under the inner trench slope and in the oceanic crust of the outer trench slope (Honza, 1981).

These features are in contrast to the characteristics of mostly offshore earthquakes in the Tohoku backarc area, where shallow earthquakes with horizontal compressional force are dominant, leading to active thrusts on the surface (e.g. Fukao and Furumoto, 1975; Tamaki and Honza, 1985). Some great and large earthquakes are considered to have occurred in the shallow crust along the continental slope and the inner trench slope of the Tohoku and southwestern Kurile arcs, although determinations of the foci of these earthquakes are somewhat ambiguous. The accurate investigation of focal depths by deployment of ocean bottom seismograph (OBS) arrays suggest a little different conclusion, that there is less seismic activity in the shallower regions (Hirata et al., 1985; Nishizawa et al., 1990). Focal depths determined by the OBS arrays are approximately 20 to 40 km deeper than those by land networks (Nishizawa et al., 1990).

Tsunami source areas in the Japan Trench and the southwestern Kuril Trench regions were outlined by sea wave refraction methods using data from old documents and recent instrumental recordings (Hatori, 1976). The results suggest that the hypocenters are in the inner trench slope and in the continental slope of the Japan Trench and the southwestern Kuril Trench regions (Figure 1).

The submarine geological structure of the Tohoku and southwestern Kuril forearc regions was mapped on the basis of seismic reflection profiling spaced every 15 nautical miles and on sampling recovered from ocean bottom coring and drilling (Honza et al., 1978), (Figure 1). Some of these surveys in the Tohoku forearc were multi-channel seismic reflection type (Scientific Members of the Operation, 1979). On the basis of these data, the Deep Sea Drilling Project (DSDP) planned and carried out drillings in the northern Tohoku forearc (Scientific Party Legs 56, 57, 1980).

In this paper we attempt to correlate epicenters of shallow earthquakes with active faults which were detected by seismic reflection profiling and to define structural blocks from the geology of the forearc.

Geological Setting of the Japan Trench and Southwestern Kuril Trench Regions.

The continental slope along the Japan Trench region is covered by Neogene sediments

(unit a in Figures 2 and 3) with thickness from one to a few kilometers (Fig. 2, L25-L5). Upper Cretaceous sediments (unit c in the Figures) underlie the Neogene sediments (Scientific party, Legs 56, 57, 1980). Throughout the region Neogene sediments unconformably overlie the Upper Cretaceous sediments in the lower continental slope. The Upper Cretaceous sediments beneath the Neogene sediments appear to have developed along the entire continental slope area of the Japan Trench region, an interpretation based on reflection profiles. Thin Paleogene sediments (unit b in the Figures) are expected to occur beneath the Neogene sediments in the northern and southern upper continental slope areas (Komatsu et al., 1981).

Faults do not tend to develop in the continental slope, except in the northern slope off Hachinohe where some minor normal faults were found in topographic highs formed by the bending of the Neogene sediments. These normal faults offset only the Neogene sediments or at most the upper most part of the Cretaceous sediments. Some faults may occur along the shelf area of the southern Oshika Peninsula (Figure 2, L13 and L15). These faults would be extensions of known on-shore faults. In the upper continental slope off Hachinohe (Fig 2, L23) a fault may occur in the Cretaceous and Paleogene sediments, but no fault was found in the Neogene sediments. The profiles showed only ponded Quaternary sediments in a depression. The smaller number of young faults in the offshore Tohoku forearc as compared to on-shore forearc and backarc where many young faults have developed is a distinctive feature. Some faults developed in the southern continental slope of the Japan Trench region (Fig 2, L5) and they are ten to twenty kilometers long.

The Neogene sediments in the continental slope extend over the trench slope break to the inner trench slope where their layering sequence become deformed by thrusts at the mid-section of the inner trench slope (Fig. 3). The thrust separates the layered sediments on the landward side from the deformed or imbricated sediments on the seaward side. The seaward imbricated sediments constitute a subduction complex associated with accretion in the lower trench slope (Honza, 1981). The Upper Cretaceous sediments cannot be traced seaward beyond the main thrust. This structural gap is also supported in refraction surveys (Asano et al., 1981). However the Neogene sediments can be traced seaward beyond the main thrust forming deformed and imbricated features. The upper most sediments have maintained a depositional pattern since the late Miocene (Scientific Party Legs 56, 57, 1980). A few additional thrusts appear to have developed throughout the subduction complex from the surface to the upper boundary of the subduction slab (Fig. 3). The horizontal extension of these faults is approximately 10 to 15 km. Imbricated thrusts are a dominant feature among these thrusts.

The southern offshore extension of the north-south trending Hidaka Belt (cf. Figure 4), which is traceable throughout central Hokkaido, bounds the northern margin of the Japan Trench. The offshore extension of the Hidaka Belt consists of highs, where an uplifted acoustic basement with some faults is observed (Fig. 2, L46). Structural trend of the high in the continental slope is also suggested to be N-S or NNW-SSE (Honza et al., 1978). The high is bound on the east side by the Kushiro submarine canyon. The trend of the faults in the belt is not ascertainable because of the width of spacing of the survey lines but we can infer that the faults in the belt trend NNW-SSE as the highs and lows in the belt have a tend parallel to the trend of the belt.

The continental slope of the southwestern Kuril Trench on the east side of the Hidaka Belt is steeper than the slope in the Japan Trench and is covered with relatively thin Neogene

sediments, as compared to that of the Japan Trench (Fig. 2, L43-L31). The deposition of thin Neogene sediments may suggest less supply of sediments from on-shore areas adjoining the southwestern Kuril Trench region. Some reverse faults or thrusts have developed in the mid-section of the continental slope. These faults are in water depth range from 2000 m to 4000 m. The faults are parallel to the trench and have sea-bottom surface expressions of 30 to 70 km. The southwestern Kuril Trench is in contrast to the Japan Trench where no reverse fault or thrust has been observed in the continental slope area.

Shallow Large Earthquakes and their Relation to Geological Structure

Twenty shallow large earthquakes with magnitudes greater than 6.5 and with foci less twenty kilometers deep have occurred in the interval between 1951 and 1989 in the Japan Trench and the southwestern Kuril Trench regions according to the JMA record listed by Ishikawa (1986). Shallow earthquakes since 1951 were selected because they have reliable hypocenter solutions and because they correlate well with known active faults (Table 1). Most earthquakes in Table 1 are on the continental slope or on the inner trench slope of the trenches. The earthquakes tend to concentrate in the area offshore from Sanriku and in the area offshore from Erimo Point.

The correlation between shallow earthquakes and faults in the northern section of the Japan Trench suggests that many shallow earthquakes have occurred in this area, despite the absence of large faults on the continental slope (Fig. 2). The detection of micro-earthquakes in the crust of the Tohoku forearc by OBS arrays (Nagumo et al., 1976; Hirata et al., 1985), suggests that some small faults may have developed in this area. It is notable that the hypocenters of micro-earthquakes occurring in the upper crust in the offshore Tohoku forearc determined by land networks always shift to deeper parts, reaching to the upper most layer of the subducting slab when accurately determined by OBS observations (Nishiwawa et al., 1992). This clearly suggests that the shallow large earthquakes in the crust of the Tohoku forearc were miss-located by land networks. Epicenters should shift seaward or the hypocenters should be deeper.

Distribution of large earthquakes in the subduction complex may be diffused, or perhaps there may be no large earthquake in the complex (Chen et al., 1982). Imbricated thrusts in the complex cannot be traced from one seismic profile line to the next when the distance between the profiles is about 50 km. The only possibility is the occurrence of shallow large earthquakes at the dominant thrust which forms the boundary between the layered Cretaceous and Neogene sediments. If this is the case, several earthquakes, namely numbers 16, 19, 10 and 7 of Figure 2 might have occurred there. Even then the epicenters and the faults are separated by horizontal distances of 15 to 50 km.

In contrast to the northern section of the slope, in the southern section of the slope along the Japan Trench are some reverse faults or thrusts with horizontal lengths from 10 to 50 km. They may be correlated to some shallow earthquakes. Even these faults may not be long enough to generate large earthquakes which need, at least, horizontal lengths of more than several tens of kilometers with vertical dislocation from a few to several meters. An unusual type of coupling between the Pacific plate and the Philippine Sea plate has been suggested for the

southern Japan Trench region (e.g. Hurukawa and Imoto, 1990), so that there may a different tectonic setting in the southern Japan Trench. But we cannot count on the effect of the subduction of the Philippine Sea plate to explain the existence of the faults.

There are some faults in the topographic highs on the continental slope traceable from the Hidaka Belt, where several shallow earthquakes have occurred (Fig. 2, L46). These earthquakes, numbers 2 to 5, constitute a series of main and aftershocks, which occurred from March to May in 1952. Large earthquakes in the Hidaka Belt are also diffused when correlation is attempted with geological structure. The focal mechanism solution of the main shock (Table 1, No. 2) suggests stress orientation rather parallel to the Kuril Trench (Kasahara, 1975). From the aftershock distribution of the 1982 Urakawa earthquake, a northeastward dipping plane from depth of 20 km to 30 km was noted in the western boundary of the Hidaka Belt (Iwasaki et al., 1983). These trends are not concordant with the structural trend of the Hidaka Belt.

Shallow earthquakes in the slope of the western Kuril Trench were correlated to the reverse faults or thrusts in the mid-slope area without any consideration of correlation between scale of faults and magnitudes (Fig. 2, L43 and L41). One of the faults is 60 km long and parallel to the trench. The fault might have been formed by the aftershocks while the main shock occurred in the upper most part of the subducting slab. Or perhaps a few faults may have coupled and ruptured simultaneously to generate the large earthquake. Possible coupling of faults is suggested in the 1973 Nemuro earthquake which occurred in the upper most part of the subducting slab in the southwestern Kuril Trench on 17 June 1973, in which case the aftershocks were distributed not around the main shock but to the area south of the main shock in the Kuril forearc (Suzuki, 1975). The earthquake number 14 is possibly one of the aftershocks of this main shock and may be associated to one of the reverse faults which developed in the slope area. This suggests that the faults can be traced to the upper most part of the subducting slab.

Normal faults forming horst and graben structure in the outer trench slope are considered to cause large earthquakes (Kanamori, 1971). Some of the ruptures may extend down through the entire lithosphere thickness. However most normal faults have horizontal dimensions of several tens of kilometers in the northern Japan Trench (Cadet et al., 1987) and are considered to extend to depths of about 15 km. Here again faults may couple to cause large earthquakes. At depths greater than 15 km, horizontal compressional stress is considered to be dominant, as was found to be the case in the outer trench slope of the Aleutian Trench (Frohlich et al., 1980). Some of these extended faults are inverted to thrusts beneath the inner trench slope (Fig. 3, L M4). These inversions suggest that the surficial tensional field in the outer trench slope is inverted to a compressional field when the oceanic crust is subducted under the arc.

Source areas of most historical tsunamis inferred from old documents and outlined by means of sea-wave refraction technique are concentrated in the vicinity of main thrusts which are the boundaries between the continental crust and the subduction complex (Hatori, 1976). This suggest occurrences of shallow earthquakes in these thrusts or along the shallower part of the subducting slab. Some tsunamis occurred in the Hidaka Basin where hypocenters of the generating earthquakes were located in the deeper subducting slab. Tsunamis may be generated by deformational movement of the upper crust caused by a deeper earthquake along the subducting slab, even if no fault was formed in the upper crust.

Crustal anisotropy of the Tohoku forearc is suggested by data from OBS and land network seismic observations (Suzuki et al., 1975), by results of explosion seismology at sea

(Yoshii et al., 1981), and by distribution of seismic intensity of local earthquakes (Usami et al., 1992). These investigations advanced the knowledge of the detailed seismic structure of the forearc. To promote further understanding, accurate hypocenter determinations in the forearc area by deployment of long term OBS array is strongly recommended.

Structural Blocks in the Japan Trench and the Southwestern Kuril Trench Regions

On the basis of possible shallow earthquake generation, which can be correlated to active faults,characteristic features can be grouped together to identify four structural blocks in the forearc areas of the Tohoku and southwestern Kuril regions (Figure 4). The section in the subduction complex where occurrence of large earthquakes is questionable constitutes a fifth block. A sixth block from the outer trench slope to the trench swell area can be outlined, but no large earthquake has been observed in this block since 1951. Some large historical earthquakes may have occurred in the outer trench slope area. One possible locus of occurrence is along the many thrusts which separate the landward terrigenous sediments from the seaward subduction complex.

The southwestern Kuril Trench is characterized by reverse faults or thrusts in the slope area. These faults are due not only by main shocks but possibly also by aftershocks. A few of these faults could have been coupled and ruptured simultaneously in large earthquakes. None of these faults is long enough to have generated a large earthquake by itself.

In the southern section of the Hidaka Belt, a structural trend of NNW-SSE differing from the main structural trend is evident. However earthquake distribution follows the main trend. There may be shallow earthquakes in this area, but we cannot discuss the scale of earthquakes as seismic reflection data are insufficient to estimate the dimensions of the faults.

The Japan Trench region is characterized by few faults in the upper crust. Detailed examinations of the region suggest that there may be smaller structural sub-blocks inside Block C of Figure 4 (Honza, 1974) where seismological activities differ from one sub-block to another. The difference is postulated to arise from different coupling stresses between the continent and the subducting slab (Kawakatsu and Seno, 1983). However from the point of view of the relation between earthquakes and active faults in the upper crust, Block C should not be divided into sub-blocks. The southern margin of Block C is ambiguous, but OBS array observations suggest structural features similar to the northern section of Block C offshore from Fukushima (Nishizawa et al., 1990). The southern margin of Block C is bounded by a fault which forms a canyon in the inner trench slope (Fig. 4).

At the southern section of the Tohoku forearc, Block D differs from Block C in that there are more faults and a different kind of topography forms a complicated slope structure. This may be due to effects from the subduction process of the Philippine Sea plate to the southeast.

Discussions

Although many large earthquakes have been listed by the Japan Meteorological Agency (JMA) as having occurred at shallow depths in the Tohoku forearc slope area, the number of active faults in the area are small. Even for these known faults, fault lengths are too short to

have been associated with large earthquakes of magnitude larger than 6.5. Besides, of the 20 or so large shallow earthquakes listed in Table 1, only two have generated tsunamis with wave heights greater than 1.0 m. The short fault lengths and the dearth of tsunamis suggest that these so-called shallow earthquakes actually occurred at greater depths, perhaps at the upper most part of the subducting slab. When earthquake foci calculated from OBS array data resulted in foci deeper than foci calculated from data provided by land-based seismic network (Nishisawa, 1990), it enhanced the suspicion that so-called shallow large earthquakes in this region have foci deeper than those published by JMA.

This leads to a statistical inference that in Block C, earthquakes must have magnitudes larger than 7.5 to generate damaging tsunamis, that is, tsunamis with wave heights greater than 1.0 m at the shoreline. The geophysical explanation is that earthquakes are so deep that such magnitudes are necessary to generate damaging tsunamis.

Conclusions.

Four structural blocks were identified in the Tohoku and southwestern Kuril forearc regions and others could be proposed for the subduction complex in the inner trench slope and for the region from the outer trench slope to the trench swell. The southwestern Kuril forearc block, Block A, is characterized by reverse faults or thrusts in the slope area. The submarine portion of the Hidaka Belt, Block B, is characterized by faults trending parallel to the trend of the belt in the uplifted sections. The main section of the Tohoku forearc, Block C, has less active faults than the southwestern Kuril block. The southern margin of the Tohoku forearc, Block D, is characterized by a type of subduction coupling with the Pacific and Philippine plates, a process different from those in the northern sections.

Until the JMA changes its techniques for determining foci of earthquakes with magnitudes larger than 6.5, the foci determined by JMA should be considered to be located at deeper depths, in and along the subducting slab under the continental slope area of the japan Trench and southwest Kuril Trench regions. These earthquakes will generate tsunamis, but the tsunamis will be damaging when they are generated by earthquakes with magnitudes about 7.5 or greater. This factor should be considered by emergency management officials when drawing up response plans when large earthquakes occur off the Sanriku Coast of Japan.

Acknowledgement

We would like to thank Dr. S. Iwasaki for his helpful suggestions on tsunami data.

TABLE 1.
SHALLOW, LARGE EARTHQUAKES LISTED BY JAPAN METEOROLOGICAL AGENCY, 1951 - 1995

	YEAR-DATE	TIME	LATITUDE	LONGITUDE	DEPTH	Ms	AREA	TSUNAMI
1.	1951 Oct 18	17:26	41° 18.0'	142° 11.0'	20	6.6	E off Shimokita P.	
2.	1952 Mar 4	10:22	41° 48.0'	144° 8.0'	0	8.2	SE off Tokachi	T
3.	1952 Mar 4	10:40	42° 0.0'	144° 18.0'	10	7.1	SE off Tokachi	
4.	1952 May 10	02:03	41° 42.0'	143° 43.0'	20	6.8	SE off Erimo Pt	t
5.	1952 May 20	03:32	41° 46.0'	144° 19.0'	10	6.5	SE off Tokachi	
6.	1952 Oct 27	04:19	39° 22.0'	143°18.0'	20	6.5	Far E off Sanriku	
7.	1958 Apr 8	03:05	38° 20.0'	143° 25.0'	0	6.7	Far E off Miyagi Pref	
8.	1959 Oct 26	16:35	37° 28.0'	143° 15.0'	10	6.8	Far E off Fukushima	t
9.	1960 Mar 21	02:07	39° 57.0'	143° 26.0'	0	7.2	Far E off Sanriku	t
10.	1960 Mar 23	09:23	39° 25.0'	143° 43.0'	0	6.7	Far E off Sanriku	t
11.	1961 Jan 16	21:12	36° 13.0'	141° 59.0'	20	6.5	Far E off Ibaraki Pref	t
12.	1968 May 16	09:48	40° 44.0'	143° 35.0'	0	7.9	E off Aomori Pref	T
13.	1968 Jun 12	22:41	39° 25.0'	143° 08.0'	0	7.2	Far E off Sanriku	t
14.	1973 Jun 27	07:31	43° 05.4'	145° 49.8'	10	6.5	Off Nemuro	
15.	1975 Jun 14	03:08	42° 54.0'	147° 30.0'	0	6.5	E off Hokkaido	
16.	1979 Feb 20	15:32	40° 13.0'	143° 52.0'	0	6.5	Far E off Sanriku	t
17.	1981 Jan 19	03:17	38° 36.0'	142° 58.0	0	7.0	Far E off Miyagi Pref	t
18.	1981 Jan 23	04:34	38° 14.0'	143° 03.0'	0	6.6	Far E off Miyagi Pref	
19.	1989 Oct 29	14:25	39° 31.1'	143° 44.6'	0	6.5	Far E off Sanriku	
20.	1989 Nov 02	03:25	39° 51.3'	143° 03.4'	0	7.1	Far E off Sanriku	t

T: tsunami run-ups > 1 m.; t: tsunami run-ups < 1 m.

References

Asano, S., T. Yamada, K. Suyehiro, T. Yoshii, Y. Misawa and S. Iizuka, 1981. Crustal structure in a profile off the pacific coast of northeastern Japan by the refraction method with ocean bottom seismometers. J. Phys. Earth, 29, 267-281.

Cadet, J-P., K. Kobayashi, J. Aubouin, HJ. Boulegue, C. Deplus, J. Dubois, R. von Huene, L. Jolivet, T. kanazawa, J. Kasahara, K. Koizumi, S. lallemand, Y. Nakamura, G. pautot, K. Suyehiro, S. Tani, H. Tokuyama and T. Yamazaki. The Japan Trench and its junctiion with the Kuril Trench: cruise results of the kaiko project, Leg 3. Earth Planet. Sci Letters, 83, 267-284.

Chen, A. T., C. Frohlich and G. V. Latham, 1982. Seismicity of the forearc marginal wedge (accretionary prism). J. Geophys. REs., 87, 3679-3690.

Frohlich, C., J. G. Caldwell, A. Malahoff, G.V. Latham and J. Lawton, 1980. Ocean bottom seismograph measuremnts in the Central Aleutians. Nature, 286. 144-145.

Fukao, Y., and M. Furumoto, 1975. Mechanism of alrge earthquakes along the eastern margin of the Japan Sea. Tectonophysics, 25, 247-266.

Hasegama, A., N. Umino, A. Takagi, S/ suzuki, Y. Motoya, S. Kameya, K. Tanaka and Y. Sawada, 1983. Spatial distribution of earthquakes beneath Hokkaido and northern Honshu, Japan. J. Seismol. soc. Jpn., 36, 129-150.

Hatori, T., 1976. Propagation of tsunamis from sources off the Pacific coast of northeast Japan. Bull. Earthq. Res. Inst. 51, 197-207.

Hirata, N., T. kanazawa, K. Suyehiro and H. Shimamura, 1985. A seismicity gap beneath the inner wall of the japan Trench as derived by ocean bottom seismograph measurement. Tectonophysics, 112, 193-209.

Honza E., 1974. On crustal blocks, crustal mevement of the Pacific coast of northeast Japan. Geol. soc. Jpn., Mono. 10, 55-61 (in Japanese with English abstract)

Honza, E., 1978. Geological map of the japan Trench, 1/1 million. Marine Geol. Map Ser. 11, Geol. Surv. Japan.

Honza, E., 1981. subduction and accretion in the Japan Trench. Oceanologica Acta, sp. v., 251-258.

Hurukawa, N., and M. Imoto, 1990. Fine structure of an underground boundary between the Philippine Sea and Pacific plates beneath the Kanto District, Japan. J. Seismol. Soc. Jpn., 43, 413-429 (in Japanese with English abstract)

Ishikawa, Y., 1986. SEIS-PC, new version. Geoinformatics, Jpn., 11, 65-74.

Iwasaki, T., N. Hirata, K. Suyehiro, T. Kanazawa, T. Urabe, T. Moriya and H. Shimamura, 1983. Aftershock distributiion of the 1982 Urakawa-oki earthquake determined by ocean bottom seismographic and land observations. J. Phys. Earth. 31, 299-328.

Kanamori, H., 1971. Seismic evidence for a lithospheric normal faulting-- The Sanriku earthquake of 1933. Phys. Earth Planet. Int., 4, 289-300.

Kasahara, M., 1975. Fault model of the 1952 Tokachi earthquake, Abstract, n. 2, 90, Seismol. Soc. Jpn (In Japanese)

Kawakatsu, H., and T. Seno, 1983. Triple seismci zone and the regional variation of seismicity along the northern Honshu arc. J. Geophys. Res. 88, 4215-4230.

Komatsu, N., 1979. Offshore sedimentary basin, northeastern part of Honshu, Japan. Jour.j

Japan Assoc. Petrol Tech. 44, 268-271 (in Japanese with Engl. abstract)

Nagumo, S., J. Kasahara and S. Koresawa, 1976. Structure of micro-earthquake activity around Japan Trench off Sanriku obrtained by ocean bottom seismographic network observation. J. Phys. Earth, 24, 215-225.

Nishizawa, A., S. tomita, T. kanazawa, T. Iwasaki, H. Shimamura and H. Hirata, 1990. Hypocenter distributiion off Fukushim, HJune 1987, determined by an ocean bottom seismographic observation. J. Seismol. Soc. Jpn, 43, 403-411. (in Lapanese with Engl abstract) Scientific Members of the Operatiion, 1979. Multi-channel seismic reflection data across the Japan Trench. IPOD-Japan asic Data Ser. 3, Ocean REs. Inst. Univ. Tkyo

Scientific Party of Legs 56 and 57, 1980. Initial Report of the Deep Sea Drilling project, 56, 57. Washington D. C..

Seno, T., and B. Pongsawat, 1981. a triple-planed structure of seismcity and earthquake mechanisms at the aubduction zone off Miyagi Prefecture, northern Honshu, japan. Earth Planet. Sci. letter, 55, 25-36.

Suzuki, S., 1975. Determination of earthquake hypocenters in consideration of the lateral variation of velocity in the upper mantle beneath the island arcs of Japan, on the Nemuro-hanto-oki earthquake of 1973. J. Seismol. Soc. Jpn., 28, 181-199 (in Japanese with Engl. abstract)

Tamaki, K., and E. Honza, 1985. Incipient subduction and obduction along the eastern margin of the Japan Sea. Tectonophysics, 119, 381-406.

Umino, N., and S. Hasegawa, 1982. S detailed structure of the deep seismic zone and earthquake mechanism in the northeastern Japan arc,. J. Seismol. soc. Jpn. 35, 237-257 (in Japanese with Engl. abstract)

Usami, T., O. Hamamatsu, S. Hisamoto, T. Watanabe, R. nakamura and T. Uetake, 1992. Characteristics of earthquake in the Tohoku district, Japan, from a viewpoint of seismic intensity distribution. J. Siesmol. Soc. Japan, 45, 339-3511 (in Japanese with Engl. Abstract)

Yoshii, T., 1979. a detailed cross-section of the deep seismic zone vbenearth northeastern Honshu, Japan. Tectonophysics, 55, 349-360.

Yoshii, T., H. Okada, S. Asano, K. Ito, t. Hasegawa, A. ikami, t. Moriya, S. suzuki and K. Hamada, 1981. Regionality of the upper mantle around northeastern Japan as revealed by big explosions at sea, II. Seiha-2 and Seiha-3 experiments. J. Phys. Earth., 29, wo1-220.

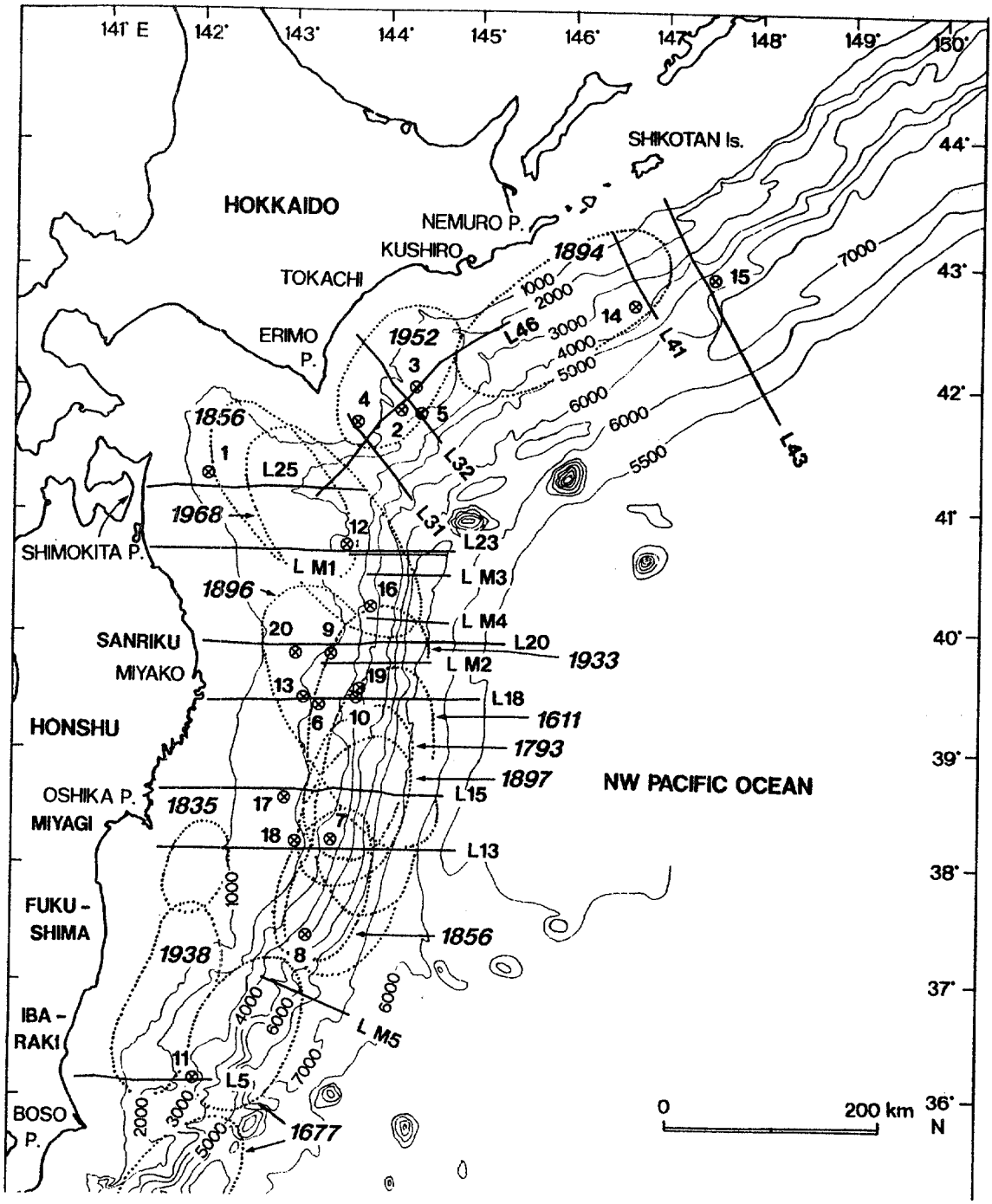

Figure 1. Track lines of single channel and multi-channel seismic reflection profiling and epicenters of large earthquakes listed in Table 1. Line numbers with M are multi-channel seismic reflection profiles. Dotted ellipses are historical tsunami source areas determined by Hatori (1976).

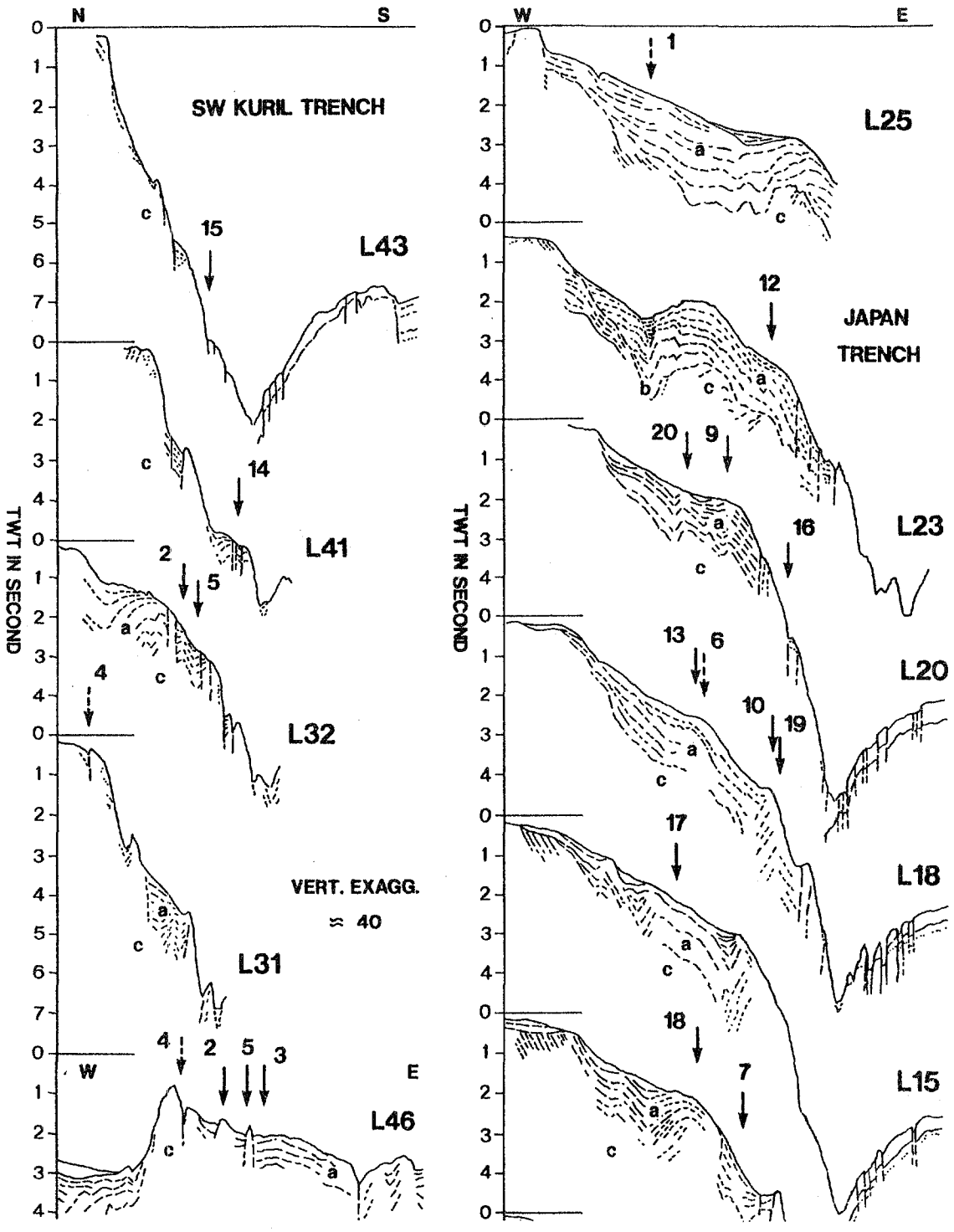

Figure 2. Single channel reflection profiles with epicenter (bar with arrow) of large earthquakes listed in Table 1. Broken bars show hypocenters at 20 km depth.

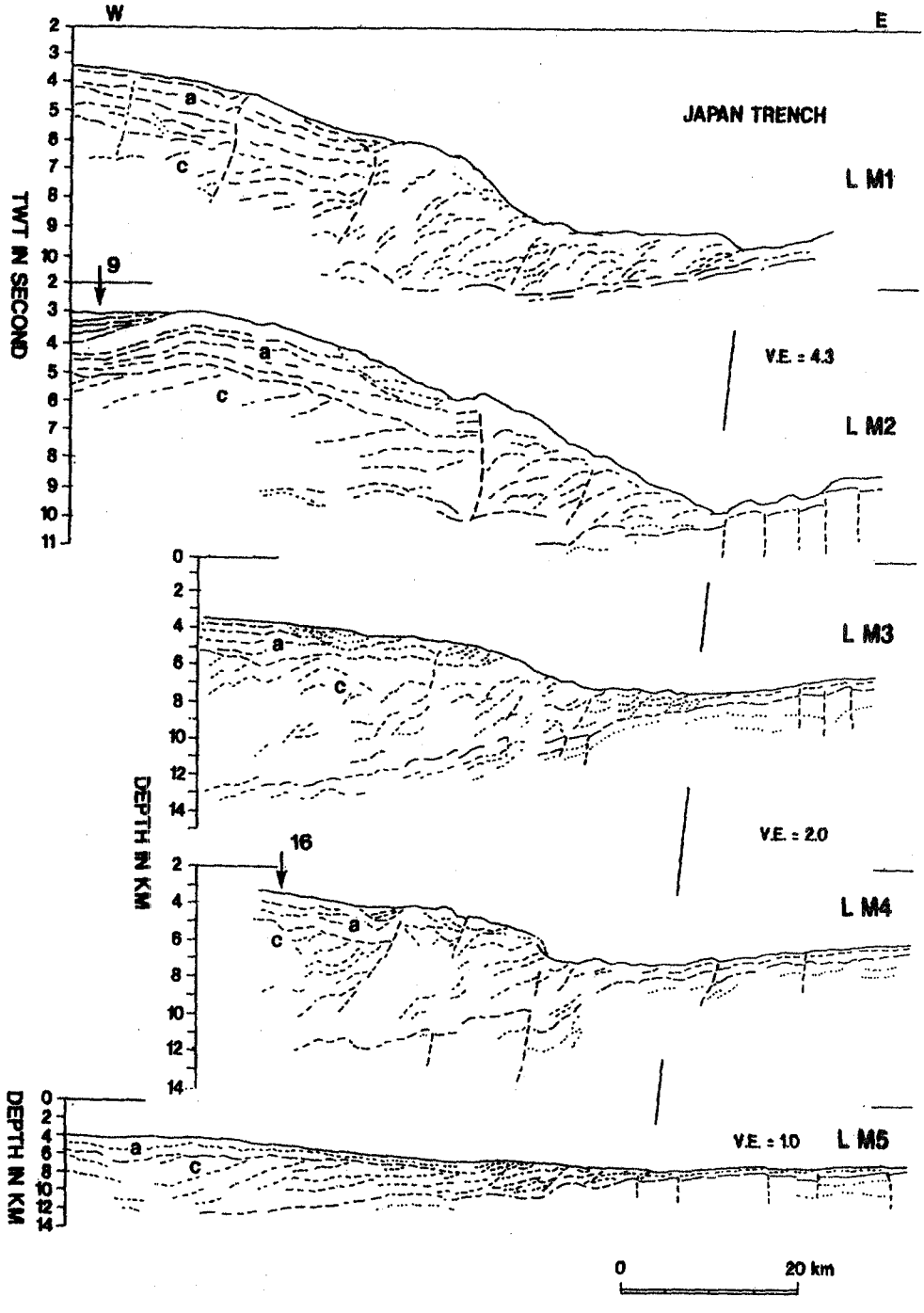

Figure 3. Multi-channel seismic reflection profiles in the northern Japan Trench. Track lines are in Figure 1.

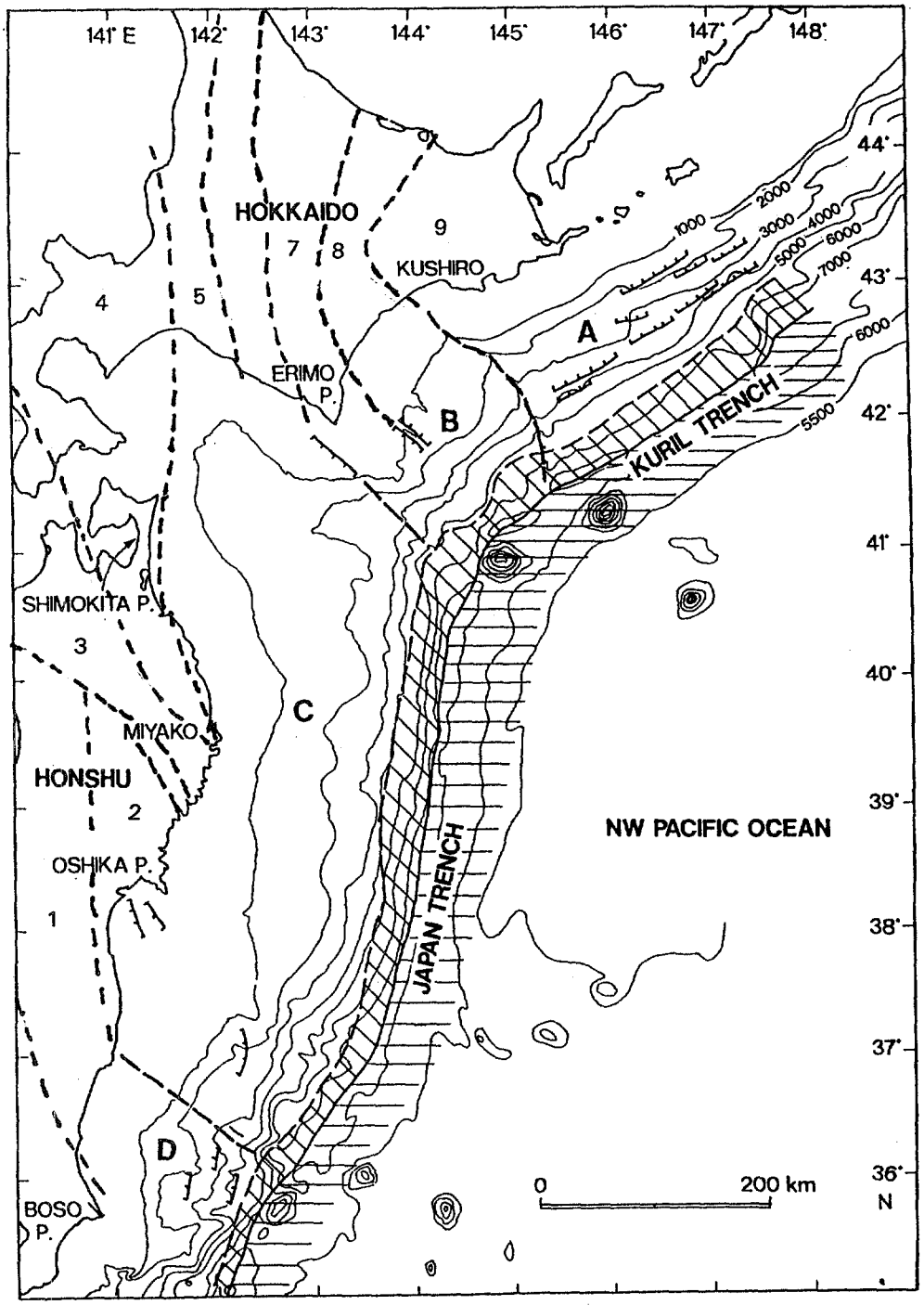

Figure 4. Structural blocks in the Jap[an Trench and southwest Kuril Trench regions. Blocks A - D are in the forearc areas bounded by broken lines. Bar with tips indicate possible active faults. The area shaded with diagonal lines is located in the subduction complex zone. Horizontal lines cover the area from the outer trench slope to the trench swell. The belts are: 1, Abukuma; 2, South Kitakami; 3, North Kitakami; 4, Iwaizumi; 5, Ishikari; 6, Kamuikotan; 7, Hidaka; 8, Tokor; and 9, Nemuro.

SCIENCE OF
TSUNAMI HAZARDS

PUBLICATION FORMAT INFORMATION

Typing area is 25 by 19 cm.

One-column text.

All text to be single-space.

Indent 5 spaces to start a new paragraph.

Page numbers in lower right hand corner in blue pencil.

Top half of first page to contain title in CAPTIALS, followed by authors and author affiliation centered on page.

Bottom half of first page to contain abstract with heading ABSTRACT centered on page.

Send original camera ready paper and a copy to

Dr. Charles Mader, Editor
Science of Tsunami Hazards
Mader Consulting Co.
1049 Kamehame Drive
Honolulu, Hawaii 96825-2860, USA

APPLICATION FOR MEMBERSHIP

THE TSUNAMI SOCIETY
P. O. Box 25218
Honolulu, Hawaii 96825, USA

I desire admission into the Tsunami Society as: (Check appropriate box.)

☐ Student ☐ Member ☐ Institutional Member

Name _____ Signature _____

Address _____ Phone No. _____

_____

Zip Code _____ Country _____

Employed by _____

Address _____

Title of your position _____

FEE: Student $5.00 Member $25.00 Institution $100.00

Fee includes a subscription to the society journal: SCIENCE OF TSUNAMI HAZARDS.

Send dues for one year with application. Membership shall date from 1 January of the year in which the applicant joins. Membership of an applicant applying on or after October 1 will begin with 1 January of the succeeding calendar year and his first dues payment will be applied to that year.